

**SEARCH FOR HEAVY PHOTONS WITH DETACHED
VERTICES IN THE HEAVY PHOTON SEARCH
EXPERIMENT**

by

Holly Szumila-Vance
B.S. May 2008, Embry-Riddle Aeronautical University
B.S. May 2009, Embry-Riddle Aeronautical University
M.S. May 2014, Old Dominion University

A Dissertation Submitted to the Faculty of
Old Dominion University in Partial Fulfillment of the
Requirements for the Degree of

DOCTOR OF PHILOSOPHY

PHYSICS

OLD DOMINION UNIVERSITY
June 2017

Approved by:

Lawrence Weinstein (Director)

John Adam (Member)

Wally Van Orden (Member)

Stepan Stepanyan (Member)

Lepsha Vuskovic (Member)

ABSTRACT

SEARCH FOR HEAVY PHOTONS WITH DETACHED VERTICES IN THE HEAVY PHOTON SEARCH EXPERIMENT

Holly Szumila-Vance
Old Dominion University, 2017
Director: Dr. Lawrence Weinstein

text of abstract goes here

Copyright, 2017, by Holly Szumila-Vance, All Rights Reserved.

ACKNOWLEDGMENTS

TABLE OF CONTENTS

	Page
LIST OF TABLES	vii
LIST OF FIGURES.....	viii
Chapter	
1. INTRODUCTION	1
2. MOTIVATION	4
2.1 THEORY OF HEAVY PHOTONS.....	4
2.2 IMPLICATIONS OF A HEAVY PHOTON	5
2.2.1 DARK MATTER	6
2.2.2 MUON G-2	6
2.3 SEARCHING FOR HEAVY PHOTONS.....	6
2.3.1 DECAY SIGNATURE	6
2.3.2 HEAVY PHOTON SEARCH STRATEGIES.....	8
2.4 HEAVY PHOTON SEARCH KINEMATICS	9
2.4.1 SIGNAL	9
2.4.2 BACKGROUNDS	11
3. HEAVY PHOTON SEARCH EXPERIMENT.....	13
3.1 CONTINUOUS ELECTRON BEAM ACCELERATOR FACILITY	13
3.2 BEAMLINE	14
3.2.1 TARGET	21
3.2.2 COLLIMATOR	22
3.3 SILICON VERTEX TRACKER	22
3.4 ELECTROMAGNETIC CALORIMETER	24
3.4.1 LIGHT MONITORING SYSTEM	27
3.4.2 AVALANCHE PHOTODIODES	30
3.5 TRIGGER	34
4. DETECTOR CALIBRATION AND PERFORMANCE	37
4.1 SILICON VERTEX TRACKER PERFORMANCE	37
4.2 ELECTROMAGNETIC CALORIMETER	37
4.2.1 SIMULATIONS	37
Energy reconstruction	38
Energy resolution	42
Position reconstruction	43
Position resolution	45
4.2.2 CALIBRATION USING COSMIC RAY ENERGY	48
4.2.3 ECAL SIGNAL PULSE FITTING	53

4.2.4	CALIBRATION USING ELASTICALLY-SCATTERED ELECTRONS	55
4.2.5	WIDE ANGLE BREMSSTRAHLUNG FOR STUDIES OF EDGE EFFECTS	56
4.2.6	ENERGY RESOLUTION IN DATA	57
4.2.7	TIMING CALIBRATION AND PERFORMANCE	60
5.	SEARCHING FOR DISPLACED VERTICES	68
5.1	DATASETS	68
5.2	MONTE CARLO SIMULATION	68
5.2.1	RADIATIVE FRACTION	68
5.2.2	VERTEX RECONSTRUCTION EFFICIENCIES, ϵ_{VTX}	68
5.2.3	MASS RESOLUTION	68
5.3	VERTEX CUTS	68
5.3.1	SVT AT NOMINAL POSITION	68
5.3.2	SVT AT OPEN POSITION	68
6.	VERTEX SEARCH RESULTS	69
6.1	BLINDED RESULTS AND PROJECTIONS	69
6.1.1	SVT AT NOMINAL POSITION	69
6.1.2	SVT AT OPEN POSITION	69
6.1.3	ESTIMATE OF CONTAMINATION BY ACCIDENTALS	69
6.2	UNBLINDED RESULTS	69
6.2.1	SVT AT NOMINAL POSITION	69
6.2.2	SVT AT OPEN POSITION	69
6.2.3	ESTIMATE OF CONTAMINATION BY ACCIDENTALS	69
6.3	REACH	69
7.	CONCLUSION	70
	BIBLIOGRAPHY	71
	APPENDICES	
	A.	73
	VITA	74

LIST OF TABLES

Table	Page
1 Pair-1 Trigger Cuts	35
2 Pair-1 trigger cut values for the Engineering Run	36
3 Horizontal position corrections.....	45
4 Position resolution.	48

LIST OF FIGURES

Figure	Page
1.0.1 Projected reach for the HPS experiment	2
2.1.1 Kinetic mixing of the SM photon with a heavy photon	5
2.3.1 The branching ratios for heavy photon decays	7
2.4.1 Heavy photon production in a fixed-target experiment	10
2.4.2 Radiative background	11
2.4.3 Bethe-Heitler background	12
3.1.1 CEBAF accelerator	14
3.2.1 HPS location in Hall B	15
3.2.2 HPS beamline	16
3.2.3 HPS magnetic fields	17
3.2.4 Charged particle trajectory in HPS beamline	18
3.2.5 HPS beamline simulation in GEMC	19
3.2.6 Beam profile from harp scan during 2015 run	21
3.3.1 Rendering of the HPS SVT	23
3.3.2 Assembly of a half module of the SVT	24
3.4.1 Drawing of the ECal assembly face	25
3.4.2 Single ECal module	26
3.4.3 Photograph of ECal crystals during assembly	27
3.4.4 LED signal in ECal FADC	29
3.4.5 Results of a single LED run	30
3.4.6 Hamamatsu S8664-3189 large area APDs	31
3.4.7 Testing assembly for large area APDs.....	31

3.4.8	APD current draw versus voltage with LED on and off	32
3.4.9	APD measured dark current as a function of gain	33
3.4.10	APD fixed gain in terms of voltage and temperature	33
4.2.1	ECal energy shower correction functions from simulation	39
4.2.2	ECal energy shower parameters for electrons relative to the inside beam gap edge	40
4.2.3	ECal energy shower parameters for positrons relative to the inside beam gap edge	41
4.2.4	ECal energy shower parameters for photons relative to the inside beam gap edge	41
4.2.5	ECal energy resolution fitted from simulation	42
4.2.6	Horizontal position correction for 1 GeV electrons	44
4.2.7	Horizontal position correction dependence for electrons	45
4.2.8	Position resolution for 1 GeV electrons.	46
4.2.9	Energy-dependent position resolution for electrons.	47
4.2.10	Setup for ECal cosmic ray calibration.	49
4.2.11	Simulation of energy deposited per ECal module from cosmic rays	50
4.2.12	Real cosmic ray signal in raw FADC waveform passing vertically through ECal	51
4.2.13	Integrated cosmic signal in ECal fitted for calibration	52
4.2.14	Resulting 2015 gain calibration in the ECal using cosmic ray muons shown by ECal module position	53
4.2.15	Distribution of the resulting 2015 gains in the ECal using cosmic ray muons .	53
4.2.16	Pulse-fitting to Mode 1 ECal data.	54
4.2.17	Reconstructed elastic peak in the ECal for the Engineering and Physics Runs	56
4.2.18	Energy resolution of the ECal found in data	58
4.2.19	Characterization of the energy resolution edge effects	60

4.2.20 Fitted, raw waveform of the RF signal in HPS	61
4.2.21 FADC intrinsic time resolution	62
4.2.22 Time difference between ECal hits and RF time.....	63
4.2.23 Time difference between two clusters after fine offset time correction	64
4.2.24 Hit times in a cluster versus the hit energy	65
4.2.25 Time walk correction for the Physics Run ECal data	65
4.2.26 Time resolution of the ECal for the 2016 run	66
4.2.27 Time resolution for the time difference between two clusters	67

CHAPTER 1

INTRODUCTION

The heavy photon, also known as the A' , is a theoretically motivated massive gauge boson that is associated with a predicted U(1) hidden symmetry, favorable to Beyond Standard Model theories. According to theory [14], a heavy photon kinetically mixes with the Standard Model photon through a loop-level effect generating an effective coupling to electric charge. This coupling to electric charge, ϵ , can range from 10^{-12} to 10^{-2} depending on loop order of the mixing interaction and describes the coupling of the heavy photon to electric charge to be at a scale significantly smaller than that in standard electrodynamic theory. While the coupling strength of the interaction can be naturally generated from the loop interactions, the mass is somewhat less constrained. Theories of the heavy photon as a way to explain cosmological phenomena make them the simplest and possible leading interaction between the Standard Model and the Dark Sector. The Dark Sector encompasses both dark matter and dark energy particles that we cannot interact with other than the observed gravitational effects. If the heavy photon should obtain its mass through the Higgs mechanism, the mass is favored to be in the range of MeV to GeV which is compatible with dark matter theories. In such a scenario, electrons could radiate heavy photons as they do ordinary photons but at a suppressed rate. These heavy photons will have measurable lifetimes before decaying to charged particle pairs. It is natural to describe the heavy photon parameter space in terms of its coupling, ϵ^2 , and mass, $m_{A'}$.

The Heavy Photon Search (HPS) experiment searches for heavy photons in the range of 20 to 1000 MeV/c² range with prompt or displaced vertices with respect to the target interaction. HPS is sensitive to heavy photons radiated from an electron beam incident on a heavy target by measuring the momentum and vertex position of $e + e^-$ pairs produced from decay. By reconstructing the invariant mass and the vertex position of the pairs, HPS can look for a small bump on a large background using a bump hunt for prompt decays. Uniquely, HPS is also able to look for heavy photons with smaller couplings (and longer lifetimes) characterized by displaced vertices by searching for a small signal on low background downstream of the target. The mass and coupling region that HPS seeks to explore is shown in gold in Figure 1.0.1 along with the existing limits from other experiments.

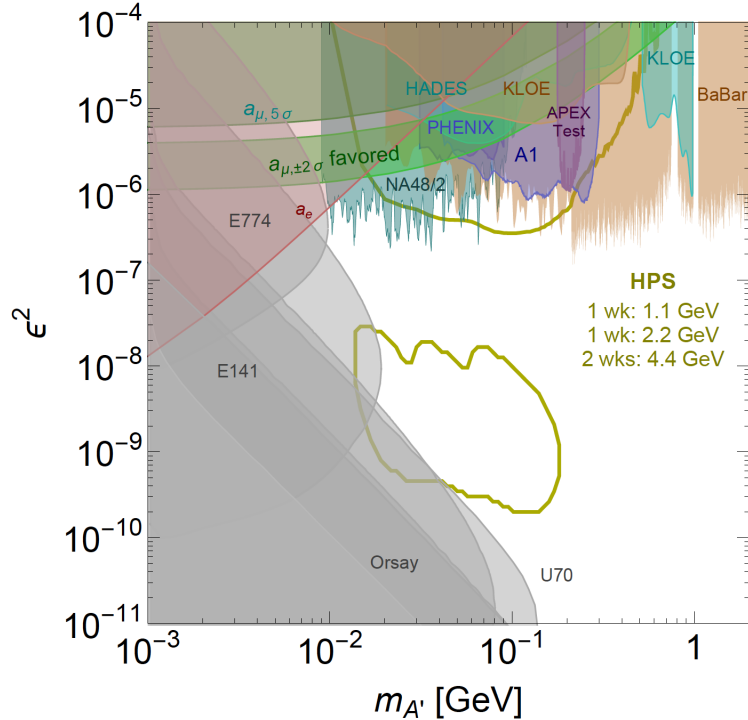


FIG. 1.0.1: The existing 90% confidence limits from other experiments looking for heavy photons in the relevant mass-coupling region is shown. The gold contours indicate the projected reach from the full running of the HPS experiment according to the proposal [?]. The green bands labeled as a_μ indicate the favored parameter space for a visibly decaying heavy photon to explain the discrepancy between the calculated and measured muon anomalous magnetic moment. The experiments along the top of the plot with large coupling look for heavy photons that decay promptly at the target. The limits shown in grey along the left side of the plot with decreasing values of coupling look for heavy photons with displaced vertices in beam dump experiments.

The HPS experiment took place in Hall B at the Jefferson Laboratory National Accelerator Facility. The Continuous Electron Beam Accelerator Facility (CEBAF) at Jefferson Lab produces an electron beam that collides with the HPS target material in Hall B. The HPS detector measures the particles from this interaction and searches for the heavy photon signal. The HPS detector consists of a Silicon Vertex Tracker (SVT) and an Electromagnetic Calorimeter (ECal). The SVT is composed of six layers of silicon strips and is housed in a magnetic field. The SVT measures particle tracks and reconstructs the vertex position of the particle pair. The ECal triggers event readout in addition to measuring particle energy and pair coincidence timing.

The ECal was commissioned during a short commissioning run in December 2014. The full experiment ran in the spring of 2015 as the official Engineering Run. This run took 2.3 days of good data at approximately 50 nA with a beam energy of 1.056 GeV. HPS obtained a total of 1529 nb^{-1} of good data. Due to the commissioning of the SVT during the Engineering Run, the SVT was not moved into its nominal position at ± 0.5 mm from the beam until later in the running, and data was taken with the SVT slightly open at ± 1.5 mm from the beam. Further experimental running took place during the spring 2016 Physics Run with a 200 nA electron beam at 2.3 GeV collecting a total of 5.7 days of data. Future running at higher electron beam energy is planned for 2018 and beyond.

This dissertation searches for heavy photons with a displaced vertex using data from the Engineering Run with the SVT at ± 0.5 mm and ± 1.5 mm from the beam. I will give an overview of the experiment as a whole with detail to the areas of which I was most involved with. Significant effort was made to study the vertex analysis in the context of a blinded analysis by using 10% of the data. In order to better understand and analyze the backgrounds in the vertex search, I conducted a detailed study of the backgrounds using the statistics of the fully unblinded dataset. In addition to the full vertex analysis, I contributed significantly to the assembly, characterization and commissioning of the Ecal for all experimental running. I wrote the clustering algorithm based on that used by the CLAS experiment Inner Calorimeter (IC) and improved simulations of the ECal detector.

CHAPTER 2

MOTIVATION

The Standard Model (SM) is the most successful theory for describing elementary particles and their interactions via the electromagnetic, strong, and weak forces in terms of gauge theory interactions. The existence of an additional U(1) hidden symmetry is not forbidden by the SM and is well-motivated as a means to access physics beyond the standard model. The heavy photon is the proposed gauge boson mediator for the consequential dark electromagnetic force that would arise from a U(1) broken symmetry. Theory has predicted that if such an interaction exists, then the SM photon and heavy photon would mix thus inducing a coupling between the heavy photon and electric charge proportional to ϵ [14]. This coupling is significant because electrons can radiate heavy photons through the same mechanism of radiating photons although at rates proportional to ϵ^2 . The primary goal of HPS and many similar experiments is to experimentally detect the heavy photon through this production mechanism. The heavy photon is additionally referred to as the A', dark photon, or U-boson.

2.1 THEORY OF HEAVY PHOTONS

The postulation for the heavy photon rests of an exploitation of allowable symmetries from the Standard Model. An additional U(1) symmetry in nature could interact with the SM through the mechanism of kinetic mixing [14]. In this model, the charge of SM particles would be shifted by some amount ϵ that is related to the strength of the new gauge boson (heavy photon or A' coupling to the SM charge. Kinetic mixing generates a coupling, ϵ through loop interactions as shown in Figure 2.1.1.

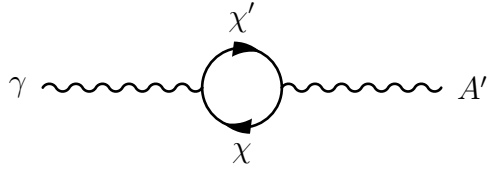


FIG. 2.1.1: Kinetic mixing of the SM photon with a heavy photon is shown at the one-loop level. *chi* can be any massive particle that is charged under both the A' and SM U(1) interactions.

In the simplest scenario, there is one particle χ that is charged under both the U(1) and new U(1) $'$. This single loop level interaction can generate the ϵ coupling to be in the range of 10^{-2} to 10^{-4} . In Grand Unified Theory (GUT), symmetries forbid one-loop interactions and favor two-loop interactions generating an ϵ in the range of 10^{-3} to 10^{-5} . [24] If both U(1)s are in unified groups, higher loop interactions generating even smaller couplings are possible. The gauge part of the SM Lagrangian is modified to include this interaction as shown in Equation (2.1.1)

$$\mathcal{L}_{gauge} = -\frac{1}{4}F^{\mu\nu}F_{\mu\nu} - \frac{1}{4}F'^{\mu\nu}F'_{\mu\nu} - \frac{1}{4}\epsilon F^{\mu\nu}F'_{\mu\nu} \quad (2.1.1)$$

In Equation (2.1.1), $F_{\mu\nu}$ is the electromagnetic field strength tensor defined in terms of the gradient of the potential as $\partial_\mu A_\nu - \partial_\nu A_\mu$. $F'_{\mu\nu}$ corresponds to the field strength of the heavy photon and ϵ is the coupling. The third term of the Lagrangian is the kinetic mixing operator. The SM photon field can be re-defined as $A_\mu \rightarrow A_\mu + \epsilon A'_\mu$ to remove the kinetic mixing operator. This generates a coupling to electric charge of order ϵ seen in the interaction between the heavy photon and SM as $\epsilon e A'_\mu J_{EM}^\mu$ where J_{EM}^μ is the electromagnetic current. [18] Particles that are charged only under the A' would not acquire this fractional charge and would remain undetectable in this model.

The mass of the heavy photon is somewhat less constrained by theory. The MeV to GeV mass scale is interesting to explore because it has been generally overlooked in previous experimentation and is consistent with dark matter theories that attempt to explain several astrophysical phenomena.

2.2 IMPLICATIONS OF A HEAVY PHOTON

Update this section with Philip's talk in May

2.2.1 DARK MATTER

Discuss excess of gamma rays at Galactic Center and focus on dark matter models in the low mass regime.

2.2.2 MUON G-2

2.3 SEARCHING FOR HEAVY PHOTONS

The final states to which the heavy photon can decay into is related to the model of the dark sector, and corresponding dark matter mass m_χ , one is considering. For a heavy photon that is heavier than m_χ , then the heavy photon may decay into completely invisible states or a mixture of invisible states and SM states. For the scenario that the heavy photon decays to completely invisible states, the experiment will perform a missing mass or missing momentum measurement in order to identify the heavy photon signal. Here, we focus solely on the scenario of a heavy photon that decays visibly to SM particles (this also implies that the heavy photon is lighter than the dark matter mass). Due to the mechanism of kinetic mixing, the production of the heavy photon is similar to that of a photon radiating from an electron although at a suppressed rate proportional to the coupling ϵ^2 .

2.3.1 DECAY SIGNATURE

The branching ratio of the heavy photon is derived from the ratios of different final state measurements of $e + e^- \rightarrow$ hadrons at various center-of-mass energies [17]. In the mass regime that HPS explores, the heavy photon can be expected to primarily decay to $e + e^-$ pairs as shown in Figure 2.3.1.

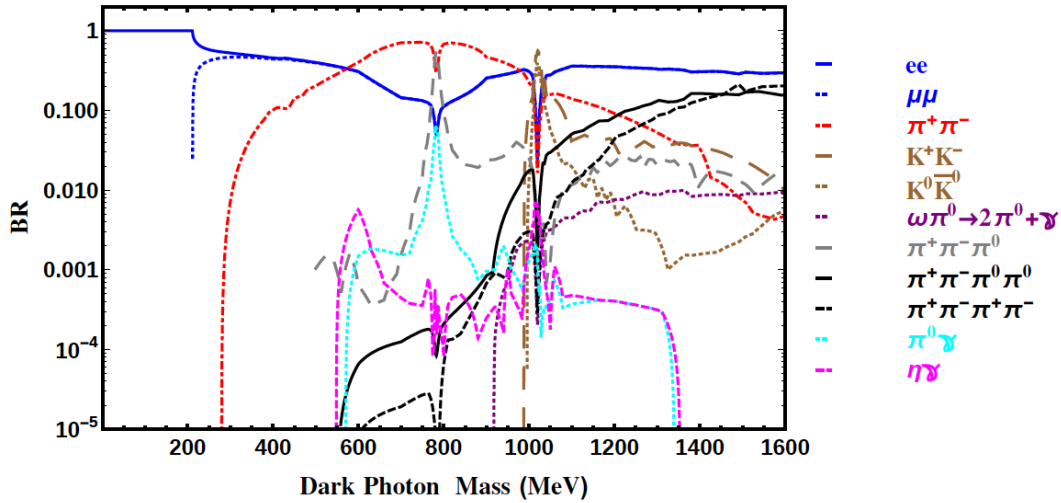


FIG. 2.3.1: The branching ratios for heavy photons of various masses. [17]

HPS searches for heavy photons of masses 20 to 100 MeV/c². As shown in Figure 2.3.1, at heavy photon masses above 200 MeV/c², the branching ratio for decays to $e + e -$ begins to decrease sharply and the turn on for decays to $\mu + \mu -$ becomes significant.

Assuming that the heavy photon only decays to SM final states, the proper lifetime of the A' neglecting phase space corrections is described by Equation (2.3.1) where N_{eff} is the number of available decay states ($= 1$ at $m_{A'} < 2m_\mu$). [18]

$$c\tau = \frac{1}{\Gamma} \simeq \frac{3}{N_{eff} m_{A'} \alpha \epsilon^2} \quad (2.3.1)$$

$$\simeq \frac{0.8 \text{ cm}}{N_{eff}} \left(\frac{10^{-4}}{\epsilon} \right)^2 \left(\frac{100 \text{ MeV}}{m_{A'}} \right) \quad (2.3.2)$$

$$(2.3.3)$$

As shown in Equation (2.3.1), the lifetime is inversely related to the coupling ϵ^2 . For small couplings, the heavy photon will travel a measurable distance after production before decaying. The decay length is described by Equation (2.3.4).

$$l_0 \equiv \gamma c\tau \quad (2.3.4)$$

$$\simeq \frac{0.8 \text{ cm}}{N_{eff}} \left(\frac{E_{beam}}{10 \text{ GeV}} \right) \left(\frac{10^{-4}}{\epsilon} \right)^2 \left(\frac{100 \text{ MeV}}{m_{A'}} \right)^2 \quad (2.3.5)$$

$$(2.3.6)$$

In Equation (2.3.4), E_{beam} refers to the incident beam energy of the electron. The rate of A' production is controlled by $\alpha^3 \epsilon^2 / m_{A'}^2$ and is suppressed relative to ordinary bremsstrahlung by a factor of $\epsilon^2 m_{e-}^2 / m_{A'}^2$. The ratio of the fully differential production cross sections for the heavy photon relative to the production of a virtual photon are described in Equation (2.3.7).

$$\frac{d\sigma(e - Z(A'Z \rightarrow l + l-))}{d\sigma(e - Z(\gamma^*Z \rightarrow l + l-))} = \left(\frac{3\pi\epsilon^2}{2N_{eff}\alpha} \right) \left(\frac{m_{A'}}{\delta m_{A'}} \right) \quad (2.3.7)$$

In Equation (2.3.7), this ratio represents the maximum signal to background that can be achieved in an experiment. The heavy photon is produced at very forward, small angles and carries nearly all of the beam energy.

Some of the formalism thus far has hinted at the production of heavy photons through bremsstrahlung-like processes of an incident electron beam on a fixed target (as in the HPS setup). However, there are other experimental processes that search for the heavy photon through other means of production. These processes include annihilations of $e + e-$ particles in collider experiments. Collider experiments are more often used for looking for heavy photons that may have invisible decay modes using missing mass measurements. Looking for heavy photons produced in meson decay channels such as Dalitz decays ($\pi^0, \eta, \eta' \rightarrow \gamma A'$) and rare meson decay channels ($K \rightarrow \pi A'$, $\phi \rightarrow \eta A'$, and $D^* \rightarrow D^0 A'$) are another production mechanism that has been used at both colliders and fixed target-type experiments. Drell-Yan ($q\bar{q} \rightarrow A'$) experiments are more common at proton fixed target and hadron collider experiments.

2.3.2 HEAVY PHOTON SEARCH STRATEGIES

The strategies for searching for heavy photons are typically a bump hunt on the visible final state particles, a bump hunt on the missing mass (assumes that the heavy photon is not always decaying visibly), or a detached vertex search for heavy photons with small couplings.

The bump hunt search on visible decays looks for a resonance on the reconstructed invariant mass spectrum of the final state pairs. The strongest limits from these experiments come from the NA 48/2, A1, and BaBar experiments ruling out most of the parameter space with couplings larger than 10^{-3} . The NA-48/2 experiment at the CERN HPS collects large samples of kaons and searches for a heavy photon produced in these meson decay channels [19]. The A1 experiment reconstructed $e + e-$ pairs in the Mainz Microtron spectrometers [20] and significantly ruled out the heavy photon as a explanation to resolve the muon $g - 2$

anomaly. Bump hunt searches can also set limits on large heavy photons with large couplings by searching the missing mass spectrum for a resonance. BaBar, an experiment at the Stanford Linear Accelerator (SLAC) $e + e -$ collider, set limits by searching for the A' in missing mass around the $\Upsilon(2S)$, $\Upsilon(3S)$, and $\Upsilon(4S)$ resonances.

The bump hunt searches are complemented by the beam dump searches that look for heavy photons with long decay lengths. The beam dump experiments E141 and E137 at SLAC, E774 at Fermilab, and one at Orsay [?] were originally run to look for MeV-mass axion-type particles from electron beam dumps. [22] The results of these experiments were later re-interpreted to set limits on heavy photons with small masses and longer decay lengths.

2.4 HEAVY PHOTON SEARCH KINEMATICS

The HPS experiment sends an electron beam onto a thin tungsten target and looks for radiated heavy photons in the reconstructed $e + e -$ mass spectrum. HPS looks for heavy photons in the range of 20 to 1000 MeV/c² and covers this territory with two searches on the same dataset that probe different heavy photon coupling regimes. A bump hunt searches for the heavy photon signal as a resonance on a large background. The bump hunt looks for heavy photons with large couplings and decay at the target. The vertex search looks for heavy photons that have detached vertices, having a measurable lifetime and decaying downstream of the target.

2.4.1 SIGNAL

The heavy photon is generated from the electron beam interaction with a heavy target as shown in Figure 2.4.1 where Z is the atomic number corresponding to the target material.

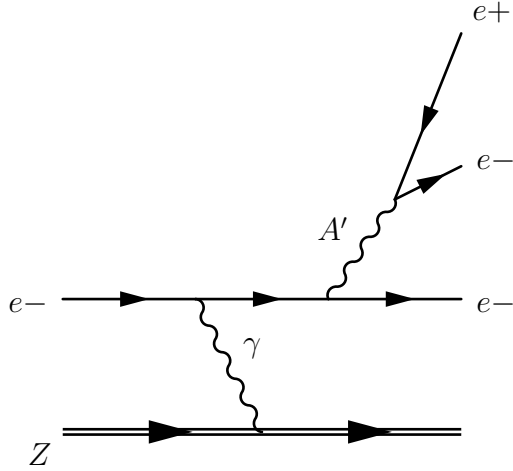


FIG. 2.4.1: The heavy photon is produced in a process analogous to bremsstrahlung on a heavy target of atomic number Z .

Shown for the HPS experiment, the heavy photon decays to $e+e-$ pairs with a measurable mass and possible displaced vertex downstream from the target. The differential cross section for heavy photon production is described in terms of the electron beam incident energy E_0 , heavy photon mass $m_{A'}$, and fraction of incident beam energy carried by the the heavy photon $x \equiv E_{A'}/E_0$ in Equation (2.4.1) [18].

$$\frac{d\sigma}{dxd\cos\theta_{A'}} \approx \frac{8Z^2\alpha^3\epsilon^2E_0^2x}{U(x,\theta_{A'})^2} \log \left(\left(1 - x + \frac{x^2}{2}\right) - \frac{x(1-x)m_{A'}^2E_0^2x\theta_{A'}^2}{U(x,\theta_{A'})^2} \right) \quad (2.4.1)$$

In Equation (2.4.1), Z is the atomic number of the target material, α is the usual fine structure constant, $\theta_{A'}$ is the lab frame angular difference between the incoming electron and outgoing heavy photon. The virtuality of the intermediate electron is described by Equation (2.4.2).

$$U(x,\theta_{A'}) = E_0^2x\theta_{A'}^2 + m_{A'}^2 \frac{1-x}{x} + m_e^2x \quad (2.4.2)$$

where m_e is the mass of the electron. The cross section is further simplified for $m_e \ll m_{A'} \ll E_0$ and $x\theta_{A'}^2 \ll 1$. Integrating Equation (2.4.1) over the angle, the cross section is shown in Equation (2.4.3).

$$\frac{d\sigma}{dx} \approx \frac{8Z^2\alpha^3\epsilon^2x}{m_{A'}^2} \left(1 + \frac{x^2}{3(1-x)} \right) \quad (2.4.3)$$

The total heavy photon production rate is controlled by $\alpha^3\epsilon^2/m_{A'}^2$ and is suppressed to photon bremsstrahlung by $\epsilon^2m_e^2/m_{A'}^2$.The singularity is regulated by the mass of the electron and cutoff for values where $1-x$ exceeds $m_e^2/m_{A'}^2$ or $m_{A'}^2/E_0^2$. The heavy photon signal carries

nearly the entire beam energy such that the median value of $1 - x \sim \max\left(\frac{m_e}{m_{A'}}, \frac{m_{A'}}{E_0}\right)$. The heavy photon is emitted predominately at small angles with a cutoff at $\frac{m_{A'}^{3/2}}{E_0^{3/2}}$ such that the angular emission falls off as $1/\theta_{A'}^4$.

The heavy photon signal is characterized by its mass (as reconstructed from the decay to $e + e-$) and decay length. Depending on the coupling strength ϵ , the vertex may be reconstructed from a prompt decay at the target or a measurable decay downstream.

2.4.2 BACKGROUNDS

The primary backgrounds in this experiment include trident events and wide angle bremsstrahlung (WAB). The tridents are broadly categorized into radiative and Bethe-Heitler diagrams are characterized by a three particle final state $e - e - e+$ [18]. The trident events were the primary source of background considered prior to the running of the experiment. It was found after experimental running that WAB events contributed to the background with an $e - \gamma$ final state where the photon pair produced to $e + e-$. In most cases, the event was triggered by the initial electron and pair-produced positron.

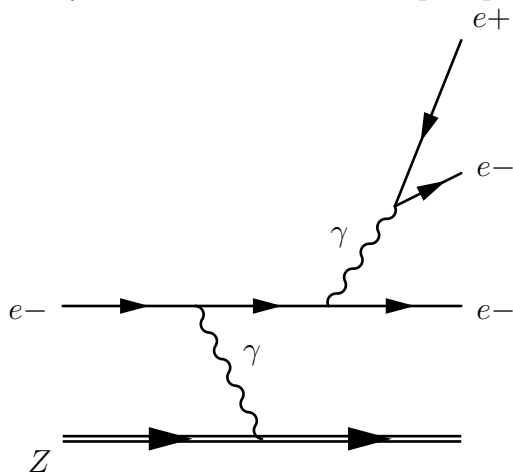


FIG. 2.4.2: The radiatives have the same kinematics as the heavy photon and comprise the primary background in the bump hunt analysis where all decays are prompt. The photon is radiated from the electron incident on a heavy target of atomic number Z and produces and $e + e-$ pair.

The radiative background is irreducible and comprises the smooth background upon which the bump hunt search for the heavy photon signal is conducted. The Bethe-Heitler tridents also contribute significantly to the background at high energy sum although they

are peaked at low energy sum. The Bethe-Heitler contribution is shown in Figure 2.4.3.

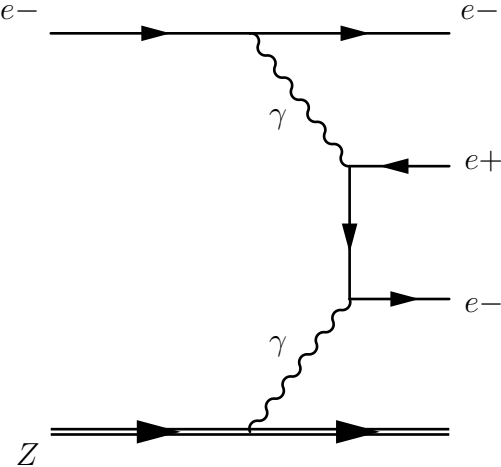


FIG. 2.4.3: The Bethe-Heitler process has a higher production higher than the radiatives but can be reduced by requiring that the energy sum of the $e + e^-$ pair be close to the beam energy. Additional contributions are considered when the recoil electron and the Bethe-Heitler positron are detected. The electron interaction with a target of atomic number Z is shown above.

The trident backgrounds also produce interferences between the radiative and Bethe-Heitler diagrams although these generally only contribute at an $e + e^-$ pair energy sum much less than the beam energy.

CHAPTER 3

HEAVY PHOTON SEARCH EXPERIMENT

The HPS experiment detector setup consists of the SVT and ECal. The SVT, located inside of a dipole magnet, measures particle momentum and vertexes $e+e-$ pairs. The ECal triggers the readout of physics events and measures particle energy and time.

The HPS experimental setup is located in the downstream alcove of Hall B at Jefferson National Accelerator Facility. CEBAF produces an electron beam which passes through Hall B to the alcove where the beam interacts with the HPS target housed inside the pair spectrometer magnet with the SVT. This interaction yields particle pairs and beam scattered electrons which pass through the six layers of the SVT before depositing their energy in the ECal for event readout.

3.1 CONTINUOUS ELECTRON BEAM ACCELERATOR FACILITY

CEBAF (Fig.3.1.1) generates the electron beam used in the HPS experiment. CEBAF is an accelerator characterized by its nearly continuous duty cycle and ability to provide electron beams to multiple experimental halls simultaneously. The CEBAF accelerator is a recirculating linac in the shape of a racetrack through which electron beam bunches can pass multiple times, boosted in energy with each pass, before being delivered to a specific hall.

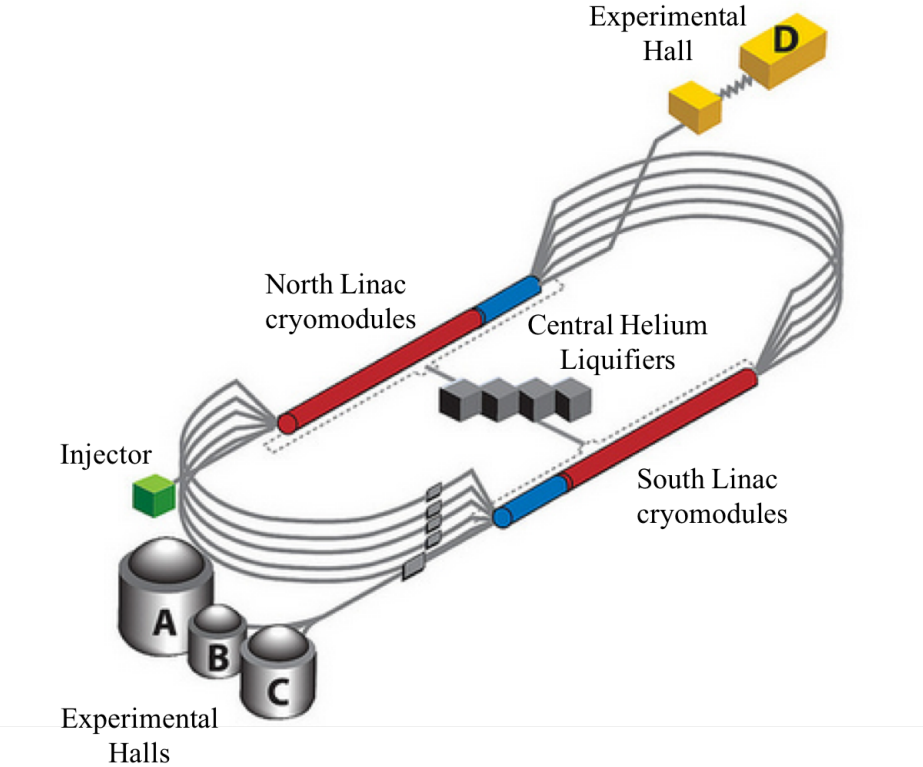


FIG. 3.1.1: The CEBAF accelerator was upgraded prior to the HPS experiment to include additional cryomodules and central helium liquifier (CHL) for higher energy, a fifth pass, and a fourth experimental hall.

The injector energy is 100 MeV, designed for a maximum of five passes (upgraded from four passes) with an energy per pass of 2.2 GeV (upgraded from 1.1 GeV). These upgrades double the maximum energy output of the accelerator. While the accelerator frequency operates at 1500 MHz, a new 750 MHz RF separator was installed in order to provide beam to all four halls simultaneously. With these upgrades, the halls can receive the beam at 250 or 500 MHz and operate at different energies [5].

HPS is the first experiment to run in Hall B after the accelerator was upgraded. After a problem occurred in one CHL during the Engineering Run in the spring of 2015, HPS obtained dedicated beam time as one of the few experiments that could continue to take physics data with the accelerator operating at a single pass using the remaining CHL. The resulting energy for the Engineering Run, 1.05 GeV, would have been impossible to obtain with the simultaneous running of other experiments requiring 2.2 GeV per pass.

3.2 BEAMLINE

The HPS experiment is installed in the downstream alcove of experimental Hall B at Jefferson Lab as shown in Fig. 3.2.1 [2]. Due to the planned construction of the CLAS12 detector in Hall B as part of the 12 GeV upgrade, HPS running was planned for nights and weekends when running beam through the hall would not interfere with CLAS12 construction. After the failure of the second CHL, HPS received dedicated, continuous running during May of 2015 in support of the Engineering Run.

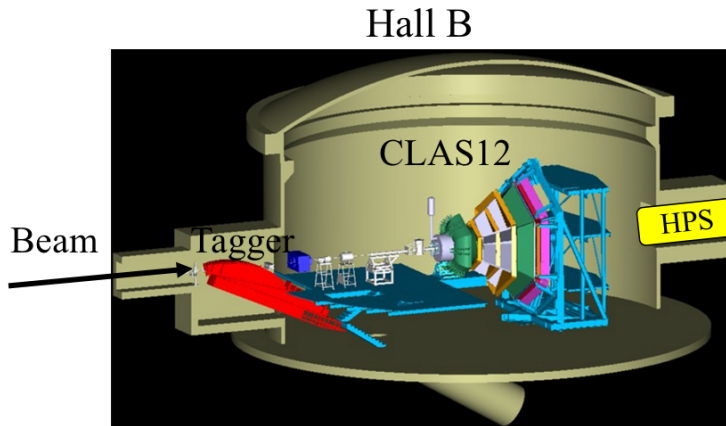


FIG. 3.2.1: The HPS experiment is in the downstream alcove of Hall B and ran while not interfering with CLAS12 construction.

The tagger magnet as depicted in Fig. 3.2.1 was used for initial beam tuning from the accelerator before sending the beam through to the HPS detectors. By energizing the tagger magnet, the electron beam was visible at the tagger dump viewer and could be aligned at the center of the viewer. Harp scans were performed to measure the position and width of the beam spot after the beam appeared to be in reasonable alignment [2]. Once the harp scans showed the beam to be of an acceptable size and position upstream of HPS, the tagger magnet was de-gaussed for HPS running. Without the tagger magnet on, the electron beam enters the hall in vacuum and passes through the hall to the HPS setup as shown in Fig. 3.2.2.

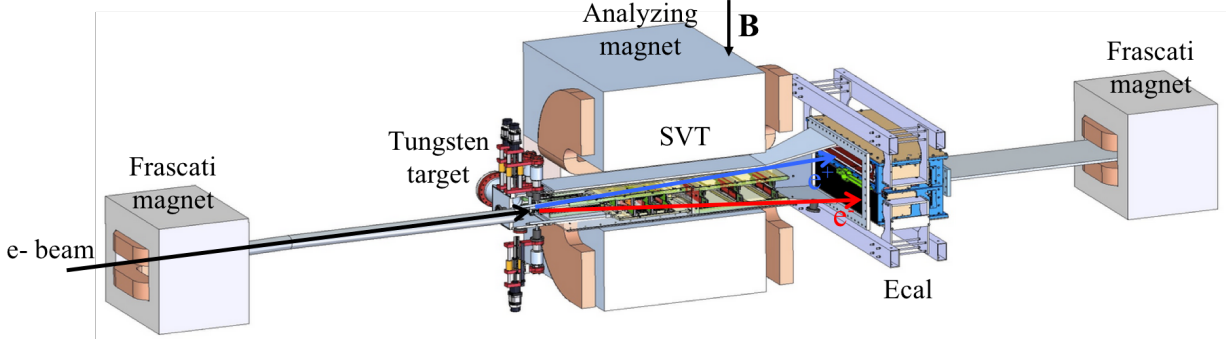


FIG. 3.2.2: The SVT and target are contained within the analyzing magnet. Particles created from the interaction of the beam at the target pass through the SVT before depositing their energy into the ECal.

The HPS setup consists of a three-dipole chicane with fields in the vertical direction, perpendicular to the Hall B floor. The target and the SVT are housed in the central magnet known as the pair spectrometer, or analyzing magnet. The pair spectrometer has a pole length of 91.44 cm and width of 45.72 cm. For 2.2 GeV electrons, the central magnetic field of the pair spectrometer magnet is 0.5 T [2]. For other beam energies, the analyzing magnet magnetic field is scaled accordingly. In the Engineering Run in May 2015, with a beam energy of 1.056 GeV, the pair spectrometer had a central field value of 0.24 T. The Frascati magnets, one on each side of the analyzing magnet, have magnetic fields opposite to that of the analyzing magnet such that the integrated field value over the length of the pole value of each Frascati is half of the integrated field value of the analyzing magnet. This ensures that the beam will end at the same location whether the chicane is energized or not and that the trajectory of beam energy electrons in the magnetic field is consistent across different beam energies. The magnetic field of the HPS beam line in the chicane is shown in Fig. 3.2.3.

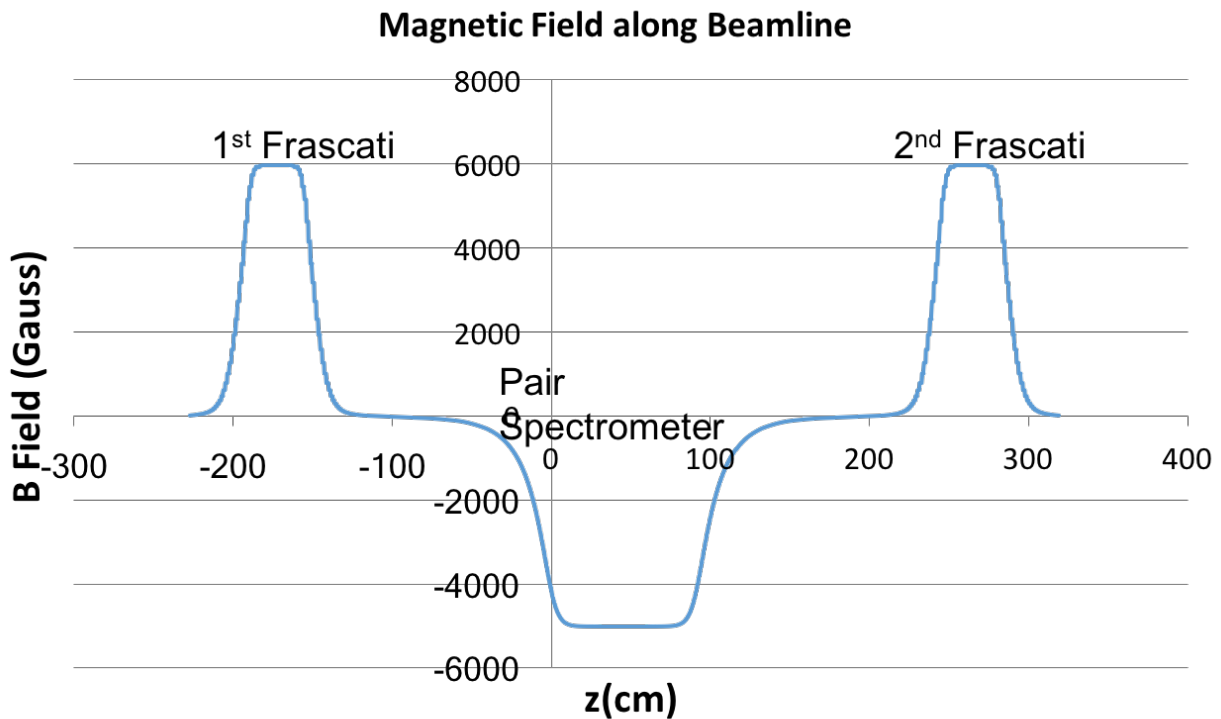


FIG. 3.2.3: The dipole field values for 2.2 GeV running.

The trajectory and position of particles inside the magnetic field was studied using magetic field mappings from experimentally obtained measurements that included fringe field effects. The positions of the pair spectrometer magnet with respect to the Frascati magnets was determined from these field mappings. The horizontal trajectory of a beam energy electron as affected by the magnetic field is shown in Fig. 3.2.4.

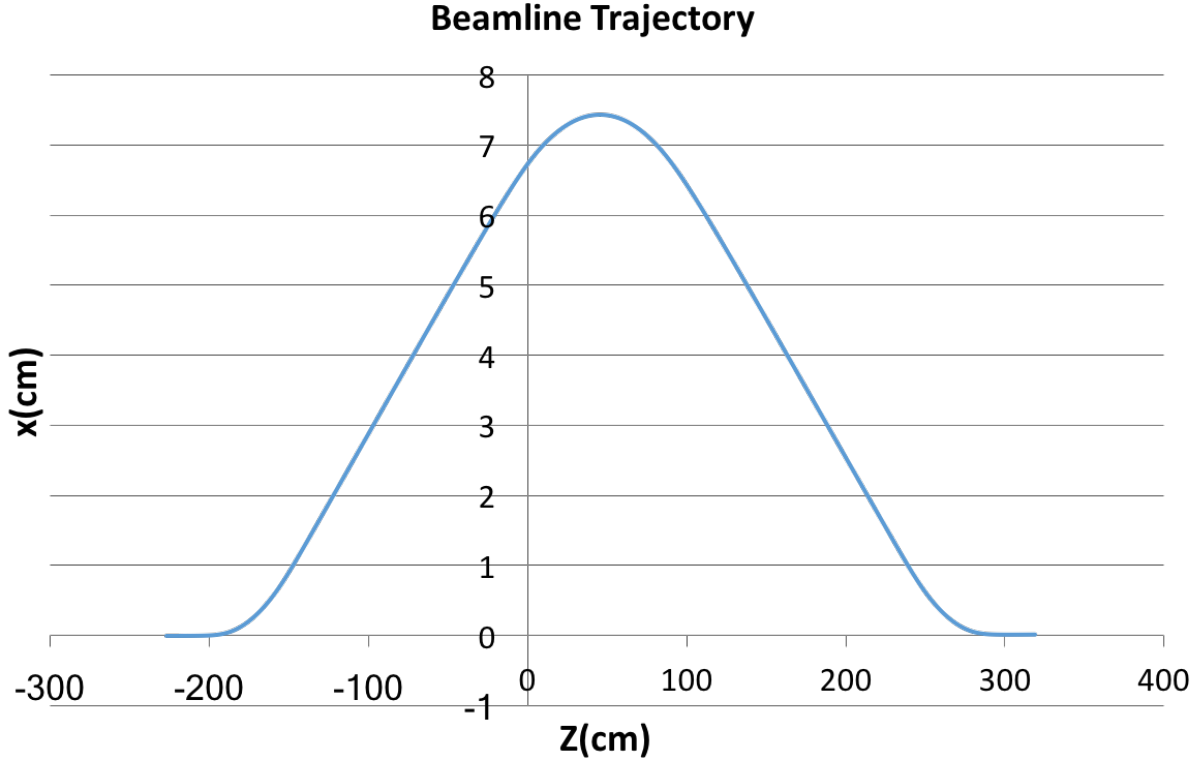


FIG. 3.2.4: The horizontal trajectory of a 2.2 GeV electron through the three dipole chicane where the target position is at $Z=0$.

In Fig. 3.2.4, the target position is where the z position is zero. The entry angle at the target was also studied and determined to be approximately 30.5 mrad. At 70 cm from the target, the pair spectrometer magnet and vacuum chamber are centered on the position of the photon trajectory from the target such that the photons pass unobstructed through all subsequent vacuum chambers. The pair spectrometer magnet was placed 8.87 cm beam left, thus placing the HPS target position 2.14 cm to the right of the magnet center line. By modeling the vacuum chambers and magnetic fields in the GEant4 Monte Carlo (GEMC) framework, the particle trajectories through the HPS beam line can be observed as in Fig. 3.2.5.

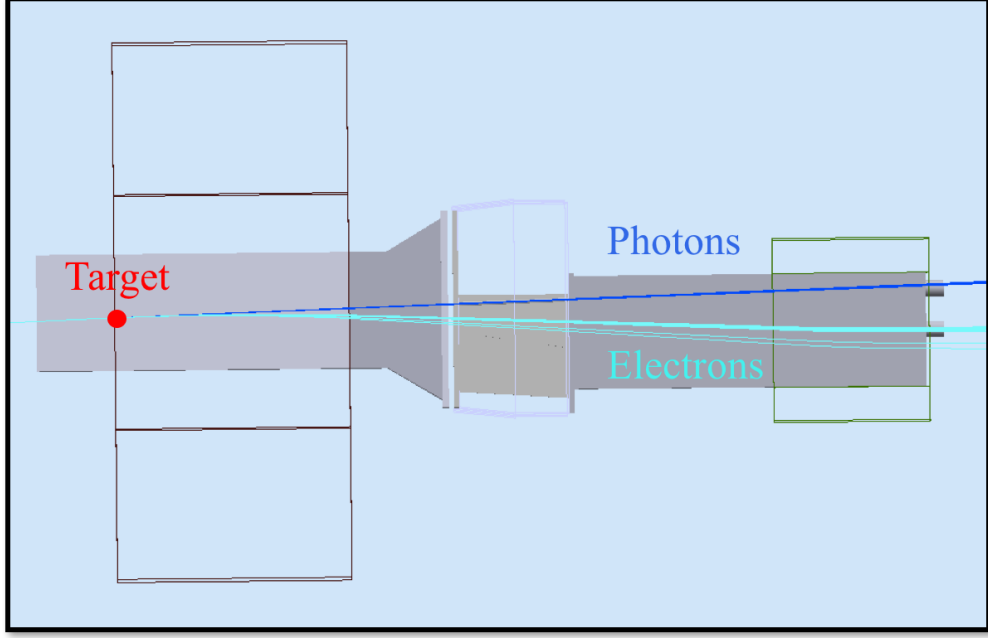


FIG. 3.2.5: A bird's eye view of the HPS beam line shows the straight line trajectory of the photons from the HPS target through the SVT, ECal, and last vacuum chamber. The trajectory of the electrons in the magnetic field can be seen as clearly passing through the relevant cut outs in the vacuum chambers.

As shown in 3.2.5, the beam energy electrons clearly pass through the exit hole of the last vacuum chamber (contained in the second Frascati dipole) and continue traveling to the Faraday cup where the beam charge can be measured. The beam line was modeled in GEMC and, in real running, utilized a multitude of monitors to ensure clear passage of the beam.

The passage of the beam through the HPS beam line was monitored using beam position monitors (BPMs), wire scans with halo counters, beam viewers, and a Faraday cup. The three upstream nA BPMs give continuous beam current and position readings. These BPMs can indicate that the beam is scraping the beam pipe when the current readings are fluctuate and differ with respect to each other. The current readings from the BPMs were compared to the current reading at the Faraday Cup (located downstream of the HPS beam line at the dump). When the beam current is at 50 nA or below, the reading at the Faraday Cup current is roughly the same as the current read out by the upstream BPMs and indicates no beam scraping in the beam pipe. When operating at currents above 50 nA, it was standard to insert a beam blocker in front of the Faraday Cup in order to protect it. The beam stopper would then create an offset in the Faraday Cup current readout and the actual

beam current. Additionally, a viewer screen at the Faraday Cup was used to show the beam position. HPS used a fluorescent screen that showed the position of the beam by emitting light at the particular point where the beam passed on the screen. A video camera streaming a view of the screen was used for remotely observing the relative beam position on the screen.

Harp scans measure the current and position of the beam through interaction with the beam (as compared to the passive, continuous readout employed through the BPMs). A harp scan moves wires through the beam vertically, horizontally, and diagonally while downstream halo counters measure the scattered beam electron spray. The halo counters are photomultiplier tubes (PMT) strapped around the beam pipe line. The intensity of the electron spray detected by the PMTs is proportional to the beam charge that the wire interacts with. A typical harp scan from the Engineering Run is shown in Fig. 3.2.6.

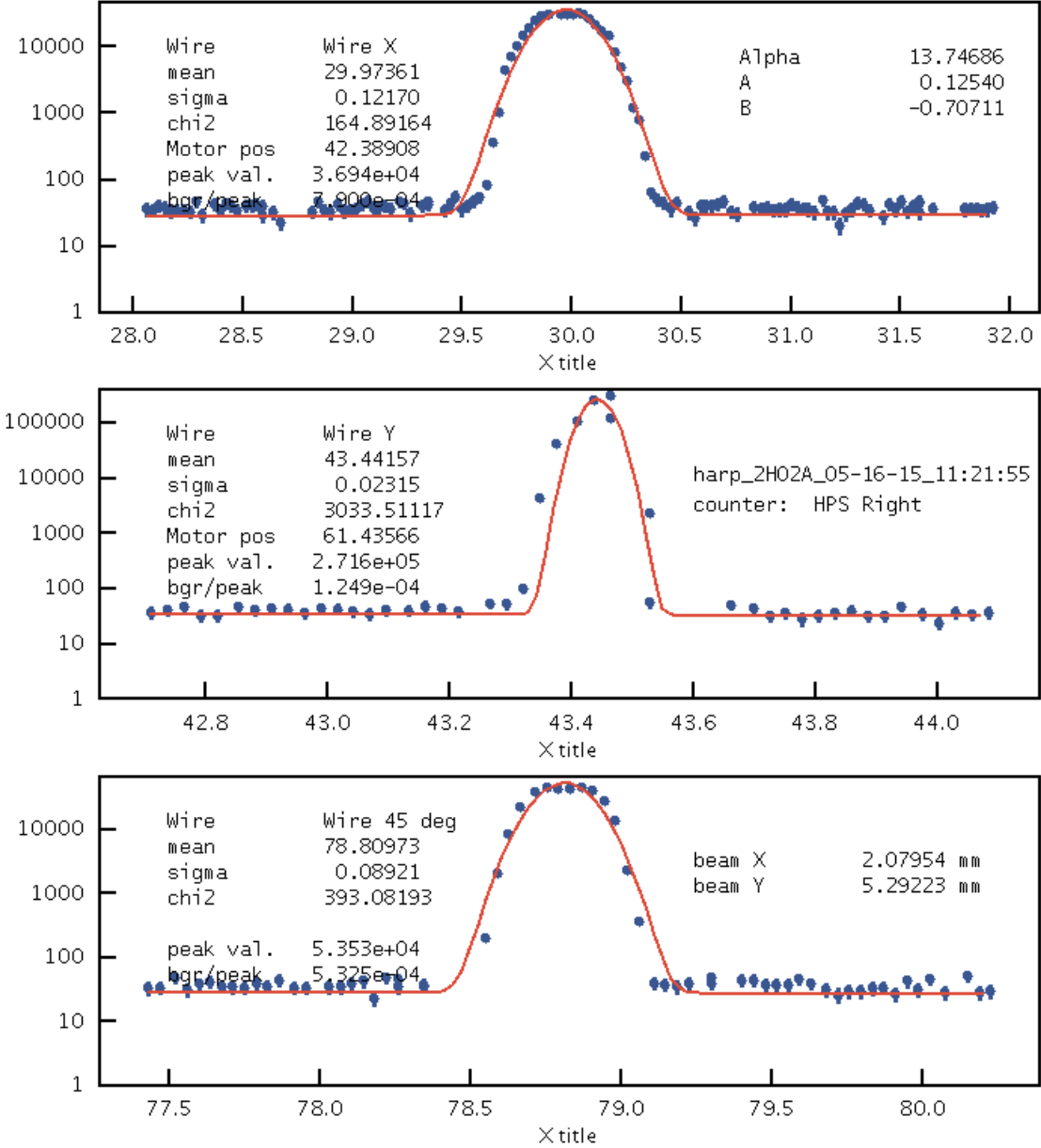


FIG. 3.2.6: Harp scan showing the beam profile during May 2015 running. This particular harp scan is in the Hall B logbook, entry 3341231. The beamline profile in this scan is 122 μm wide in x by 23 μm in y .

In Fig. 3.2.6, the beam profile is characteristically narrower in y (vertically) than in x (horizontally). The proposed beam profile for the HPS experiment was 50 μm in y and 300 μm in x in order to prevent overheating at the target and allow for precise vertex reconstruction. While overheating was not a limiting factor in the experiment, most of the 2015 running had a beam profile of no larger than 50 μm in y and 150 μm in x .

3.2.1 TARGET

The primary HPS target is a thin tungsten foil that is mounted on a support frame having the capability to be fully retracted from the beam when not in use. For proposed 1.1 GeV and 2.2 GeV running, the design thickness of the target tungsten foil is 0.125% radiation lengths (approximately 4 μm of tungsten). The measured thickness of the actual target was 0.116%. Mounted on the same frame is a tungsten target of 0.25% radiation lengths for future running at 4.4 GeV and 6.6 GeV. The target support frame inserts the foil target from above the beam using a stepping motor linear actuator. By necessity, the bottom of the target foil is free-standing so that the target can be inserted into the active beam without interruption.

3.2.2 COLLIMATOR

A collimator is used in the HPS beamline in order to protect the silicon strips of the SVT detector in the event of the beam moving vertically from its nominal position. The collimator is a 1 cm thick tungsten plate with different sized holes through which the beam can pass. Should the beam drift vertically from its nominal position, the collimator would be able to absorb the beam and protect the silicon before the machine fast shutdown (FSD) would be triggered by excess counts in the beam halo counters. For the 2015 run, the 4 mm collimator hole was used.

3.3 SILICON VERTEX TRACKER

The Silicon Vertex Tracker (SVT) is the key detector of the HPS experiment for measuring particle momentum and trajectories through a magnetic field in order to reconstruct the invariant mass and the vertex position of the $e + e -$ pair. The SVT is composed of six layers of 0.7% radiation length-thick silicon placed downstream of the target and housed in a vacuum chamber within the analyzing magnet. The SVT is separated into top and bottom halves with a 15 mrad opening angle and the first layer of the SVT at ± 0.5 mm from the active beam. A drawing of the SVT is shown in Figure 3.3.1.

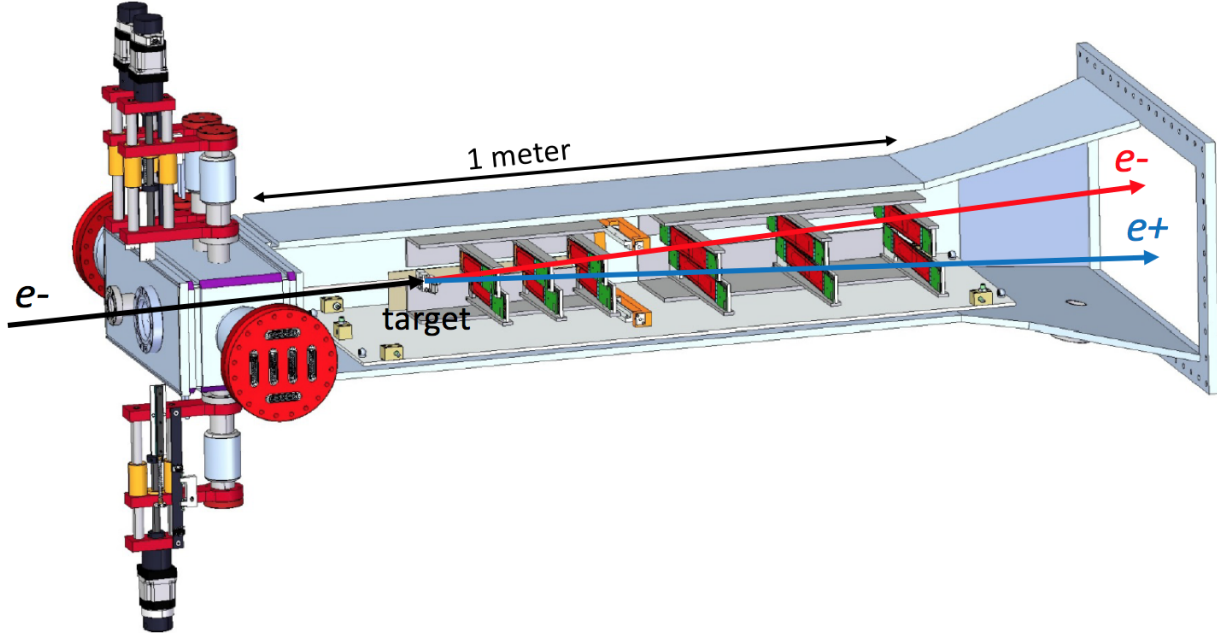


FIG. 3.3.1: A rendering of the HPS SVT. The beam enters from the left through the vacuum box. The silicon sensors are shown in red, and the hybrid readout boards are shown in green.

The SVT, as shown in Figure 3.3.1, is housed in a magnetic field such that particles are bent horizontally (field acts downward). Each of the six layers is composed of two strips capable of measuring a hit position in one dimension. By setting the strips at a stereo angle with respect to one another, each layer of the SVT is capable of three-dimensional hit reconstruction. The first three layers of the SVT are one silicon strip sensor-wide and have a stereo angle of 100 mrad between the strips. The last three layers of the SVT are two strip sensors-wide in order to better match the Ecal acceptance. The stereo angle between the sensors in layers four through six is 50 mrad. The axial sensors are oriented along the bend plane direction whereas the stereo sensors are angled with the lower end closer to the beam plane on the positron side where the background are less intense. The different stereo angles are used to eliminate ghost hits that can generate ghost tracks. The first five layers of the SVT cover the Ecal acceptance while the sixth layer has a slightly reduced acceptance but can be used to improve track reconstruction. The full track reconstruction only requires five hits per track in order to pick up tracks that may be missing hits due to an inefficiency.

The hybrid readout boards on each sensor house the APV25 readout chips that connect the sensor to the data acquisition (DAQ) system. The power to the APV25 chips is supplied through the hybrid, and the temperature of the strip is also actively monitored at the hybrid.

The heat generated by the operating hybrid is pulled out through the aluminum support structure. As the sensors are cooled for operation, the support structure and sensor contract at slightly different rates. In order to adjust and maintain the sensor at a constant tension, one end of the sensor is attached to a spring pivot in order to maintain rigidity. The assembly of a silicon sensor is shown in Figure 3.3.2.

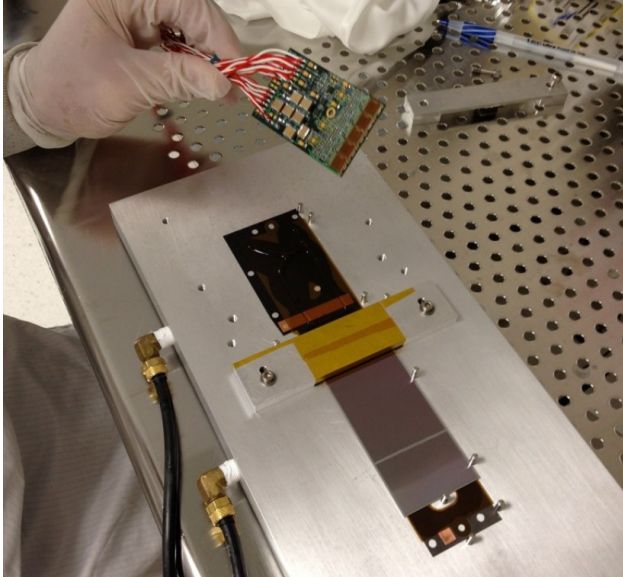


FIG. 3.3.2: A half module is being assembled for Layers 1-3 of the SVT. A readout hybrid with the APV25 chips is being attached to the frame along the silicon sensor. [4]

The APV25 samples the strips every 24 ns and stores the results in a pipeline. Once a trigger is received, the corresponding channel pipeline is readout. The readout yields six samples at 24 ns intervals that can be fit to reconstruct the waveform. A 4-pole functional fit was used to extract the time and amplitude of the corresponding hit. A latency time that is configured in the SVT DAQ is used to correctly determine which channel pipelines are readout that correspond to the trigger. The latency time is approximately equal to the time delay of the trigger. Some early data in the Engineering Run was lost due to incorrectly timing in the SVT latency.

3.4 ELECTROMAGNETIC CALORIMETER

The ECal was key for triggering events and providing particle energy and timing information during data-taking. The ECal is a homogeneous calorimeter composed for 442 trapezoidal PbWO₄ scintillating crystals each readout by a large area avalanche photodiode

(APD) attached to the back of each crystal. [1] The crystals are re-purposed from the former CLAS IC detector and have been upgraded with larger avalanche photodiodes. Each crystal is trapezoidal in shape and 16 cm long with the front (back) face $1.3 \times 1.3 \text{ mm}^2$ ($1.6 \times 1.6 \text{ mm}^2$). The calorimeter layout is shown in Fig. 3.4.1.

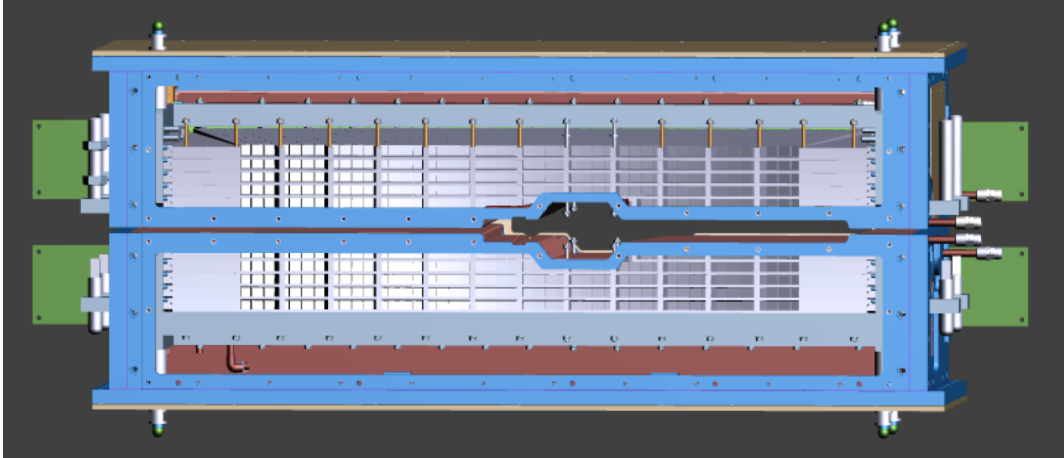


FIG. 3.4.1: Drawing of the ECal assembly face, looking downstream with the beam direction. The ECal is assembled in two vertical halves and has a gap in between allowing for the electron and photon beams as well as the sheet of flame.

The ECal is constructed as two separate vertical halves in order to avoid the 15 mrad vertical zone of excessive electromagnetic background along the beam line. The crystals in each half are arranged in five layers of 46 crystals. The layer of crystals closest to the beam in each half has nine crystals removed to allow for the passing of the electron beam. The two halves of the ECal rest at 2 cm vertical distance from the horizontal electron beam plane.

Each crystal is wrapped in a VM2002 reflecting foil in order to increase light collection. The original APDs used by the the IC had a surface area of $5 \times 5 \text{ mm}^2$, but these were upgraded for HPS running by replacing each original APD with a large area APD (model S8664-1010) of surface area $10 \times 10 \text{ mm}^2$. The upgraded large area APDs are capable of collecting four times the light as compared to the same energy deposited into the old APDs. The larger signals require less electronic amplification of the signal and improve the signal-to noise-ratio. Ultimately, the upgrade in electronics requires a lower energy threshold for module readout and improves energy resolution.

As a particle enters the ECal, it deposits all of its energy in an electromagnetic shower by either bremsstrahlung or pair production. The secondary particles then produce more particles through bremsstrahlung and photon pair production giving rise to a cascade of particles, decreasing in energy. After the electron energy is too low to yield further particles,

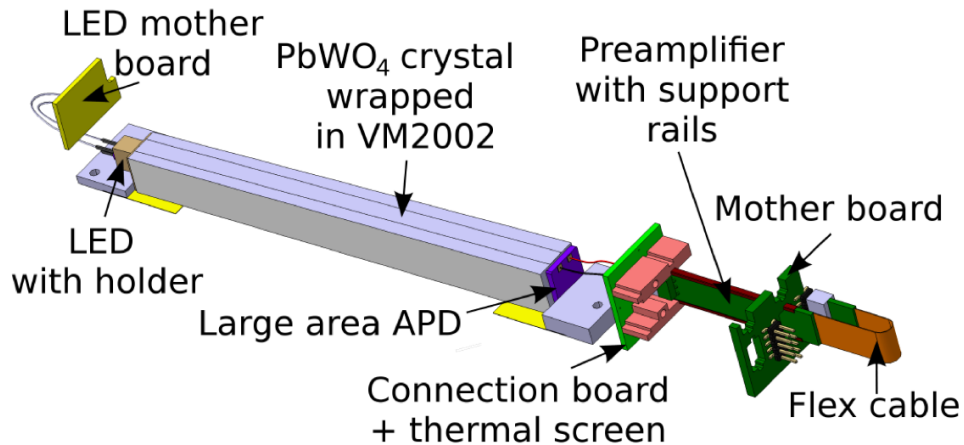


FIG. 3.4.2: Drawing of an ECal crystal in readout configuration.

the remaining energy is deposited through ionization and excitation releasing scintillation photons in the lead tungstate crystal that are gathered at the back of the crystal with an APD that converts the number of collected photons into an electronic signal via the photoelectric effect. Each APD is attached by a twisted pair connector to a preamplifier which converts the signal current to voltage and has low input impedance and noise.

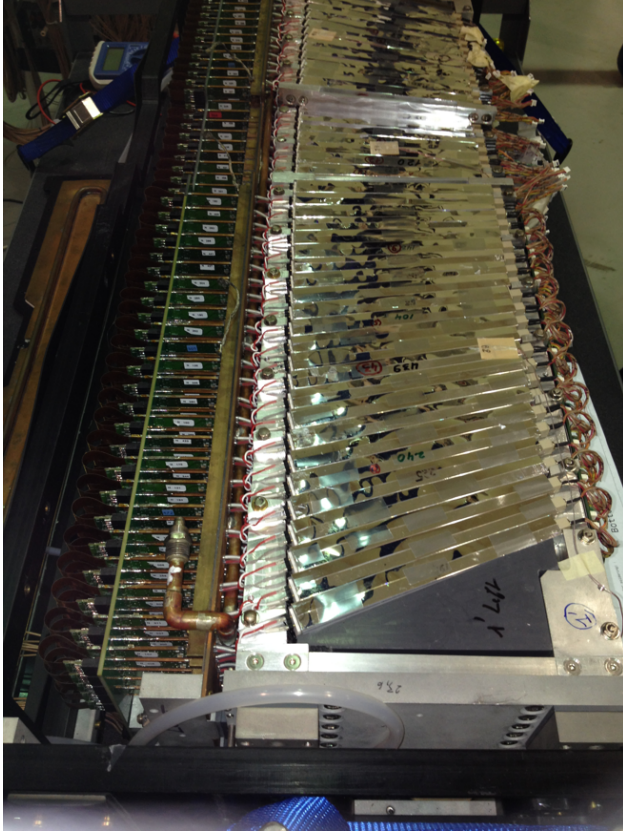


FIG. 3.4.3: Photograph taken during assembly of the ECal from above. The preamplifiers attached to each crystal are shown on the left. As single layer of wrapped crystals are shown in their tray and the LEDs attached to each crystal are shown on the right.

The gain of the APDs and the scintillation of the crystals in the ECal are temperature-dependent. An Anova A-40 external chiller operating at 17°C pumps cool water through copper cooling pipes that run along the inside of the ECal at the top, bottom, front and back face of the crystal structure. The internal temperature of the ECal was monitored using sixteen thermocouples located at various locations within the ECal structure. The thermocouples are readout using an Omega D5000 series transmitters. Both devices are connected through RS-232 serial communications for external monitoring and alarms should the temperature change significantly.

Low voltage is supplied to the preamplifiers via an Agilent 6221 operating at 5 V and approximately 4.1 A when all preamplifiers are connected. The high voltage to each of the 52 APD groups is supplied by the CAEN A1520P modules in the SY4527 mainframe. Both voltage suppliers are monitored and accessible for remote operations.

3.4.1 LIGHT MONITORING SYSTEM

The Light Monitoring System (LMS) is a remotely-controlled design upgrade addition to the ECal consisting of a bi-color LED attached to the front of each ECal module. PbWO₄ scintillating crystals are relatively radiation tolerant but have a known decrease in light yield after exposure to radiation [6]. This effect is non-uniform in the ECal as a module's geometrical position relative to the beam will result in different levels of radiation. The LMS has the ability to turn individual modules on and off independently which proved useful in checking each channel's functionality and correct cabling. The use of LEDs in a monitoring system for the PbWO₄ modules is particularly advantageous because the LEDs can be selected such that the shape and duration of the emitted flash can generate a pulse shape similar to the scintillation effect in the crystal [8].

Each crystal has a plastic LED holder glued to the front that contains a bi-color LED, model RAPID 56-0352, capable of emitting red and blue light. The use of two different colors allows for the study of different effects in the ECal modules. The blue LED has a wavelength close to the 430 nm emission peak of PbWO₄ [8] and is used to check for radiation damage in the crystal as this spectrum would be most affected. The red light is not susceptible to the radiation effects in the crystals, but is useful for checking the stability of the APD gain.

The LMS consists of four driver boards on each half of the ECal. The four driver boards on each half are connected to one of two main controllers, and each driver can turn on a single LED at a time. The controllers provide communication with the LMS through ethernet and USB interfaces. The controller board for the top half of the ECal also contains the master clock signal that sets the rate at which the LEDs flash. This clock signal is sent to the bottom controller so that the driver boards on the bottom half of the ECal can flash at the same rate, and the clock signal is used to trigger LED events when the DAQ is used.

During the initial assembly of the ECal, the LEDs were used to study the cross talk between ECal modules. The cross talk between channels was found to be at the level of $2\pm1\%$ and generally occurred in modules of the same row to the immediate left and right of the triggered module. The effect most likely appears due to light leakage out the back face of the crystal where the APD does not cover the entire surface.

The raw waveform response from a red LED signal in a single ECal module is shown in Fig. 3.4.4. The raw units are given in mV which are a factor of four times less than the units of FADC.

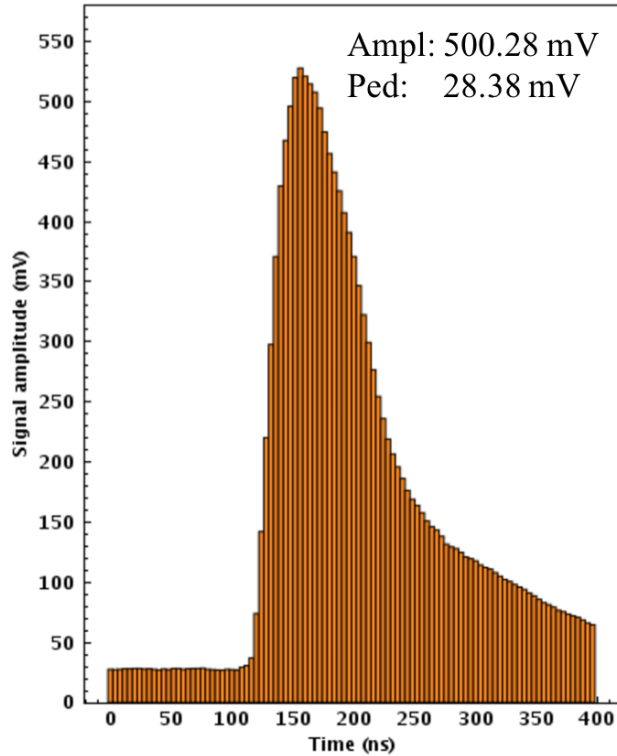


FIG. 3.4.4: A red LED in a single ECal module as readout through the FADC (see section 4.2.3)

Before and after periods of long beam run times, the ECal gains were checked with the LEDs. The LED test ran a sequence of red and blue LEDs so that the characteristic response of each module was measured. The typical results from an LED test are shown in Fig. 3.4.5.

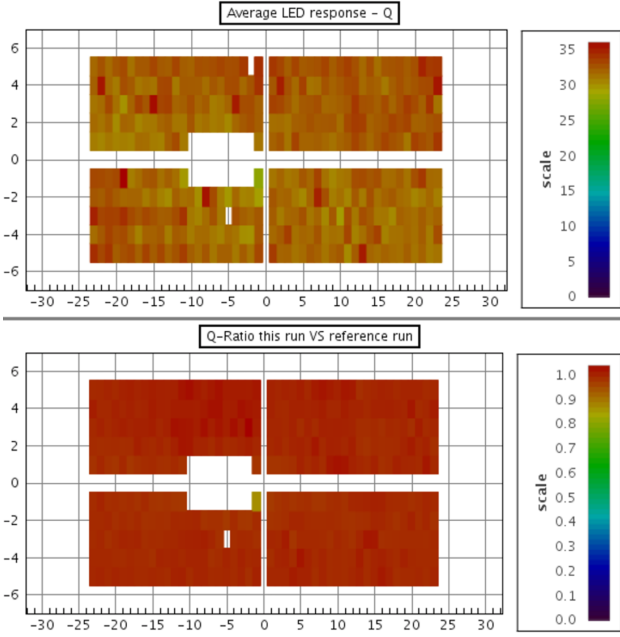


FIG. 3.4.5: The top shows the LED response in each crystal for a specific LED run. The bottom compares each crystal with its database value as stored from a previous LED run.

As shown in Fig. 3.4.5, the individual ECal module response is given as the pulse-integral in units of GeV. The response values for individual crystals have large units of energy because the LED pulse is significantly longer than an actual scintillation pulse in the crystal. A LED test can show differences in the gain of individual crystals on the order of 1% when compared to previous LED test results. During the Engineering Run, a 5% change in the gains across all modules occurred over the course of establishing production beam between February and April. This change was seen in LED response studies in addition to the gains obtained with cosmic energy calibration.

3.4.2 AVALANCHE PHOTODIODES

The ECal upgraded by installing large area Hamamatsu S8664-3189 APDs for readout. APDs were used for reading out the ECal modules due to their ability to operate in the fringe magnetic field of the HPS beam line. Both the Institut de Physique Nucléaire d'Orsay (IPN) and Instituto Nazionale di Fisica Nucleare (INFN) groups in the HPS collaboration purchased the large area APDs for upgrade. As the IPN group re-designed the motherboards for the upgrade, INFN developed the testing apparatus so that the gain of each APD could be characterized and sorted into one of 52 high voltage groups to minimize response variations. The large area APDs are shown in Fig. 3.4.6.

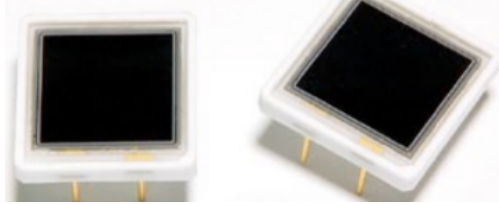


FIG. 3.4.6: The Hamamatsu S8664-3189 large area APDs.

APDs are reverse-biased diodes with an internal high electric field that multiplies the electrons through an avalanche mechanism. The characteristic gain of an APD depends on the temperature of the environment due to the interaction of the electrons with the phonons. The gain is inversely correlated with temperature. The APD gains have a linear dependence on both voltage and temperature. Prior to grouping the APDs for installation in the ECal, each APD was tested and bench marked to check for quality and optimal operating voltage in order to achieve a pre-selected gain of 150. The testing apparatus was designed and installed by the group from INFN as the same procedure was used in the construction of the Forward Tagger [7]. The bench marking apparatus is shown in Fig. 3.4.7.



FIG. 3.4.7: On the left, the testing setup is shown and includes a chiller, the light-tight plastic box that contains the LEDs and APDs, an electrometer, and the data acquisition. On the right, the setup inside of the light-tight plastic box is shown that contains a copper cooling plate to maintain the chiller temperature, 10 slots on each side to hold APDs, and the LED in the center of each half.

In order to avoid condensation on the cooling lines, the temperature range for conducting the tests was limited to 16°C, 18°C, and 20°C. During the testing, the current in each APD is measured by the electrometer with the LED on and off while stepping through a range of voltages. The measured dark and light currents for an individual APD during testing are shown in Fig. 3.4.8.

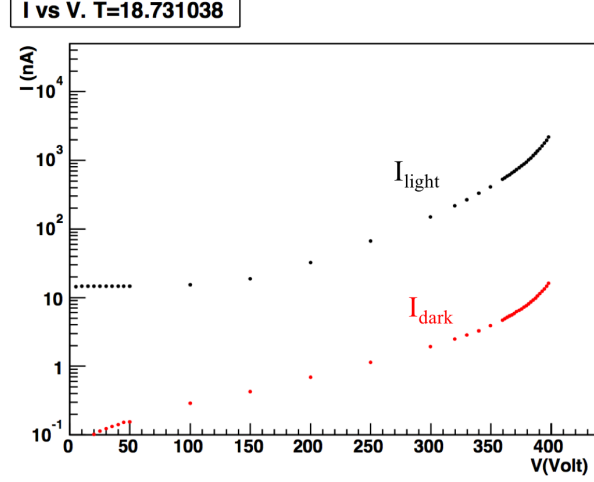


FIG. 3.4.8: The current measured from an individual APD as tested over a range of voltages with both the LED on and off. The measured temperature at the APD for this particular measurement was 18.7 °C.

The full characterization of the APD gain is calculated by the following relation:

$$Gain = \frac{I_{light}(V) - I_{dark}(V)}{I_{light}(G = 1) - I_{dark}(G = 1)} \quad (3.4.1)$$

The gain is determined to be 1 when the avalanche mechanism is not present. The $I_{light}(G = 1)$ in Eq. (4.2.10) the corresponding light current and $I_{dark}(G = 1)$ is the measured dark current when the gain is 1. Using this relation, the gain can be characterized for all measured dark currents and should have a linear relation. This relationship is shown in Fig. 3.4.9.

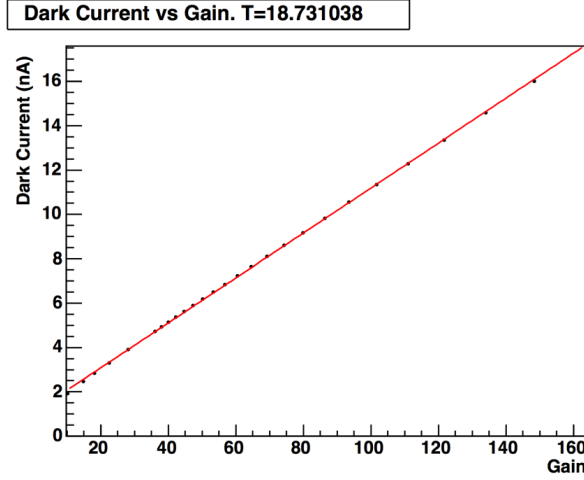


FIG. 3.4.9: The current measured from an individual APD as tested over a range of voltages with both the LED on and off. The measured temperature at the APD for this particular measurement was 18.7 °C.

If the relationship between the dark current and the gain is not linear, as shown in Fig. 3.4.9, then the APD was re-tested to ensure quality. APDs were placed into 52 common voltage groups ranging from as little as two to a maximum of ten APDs in each group in order to minimize gain variations across the ECal. The grouping temperature was chosen to be 18 °C in order to avoid condensation in the cooling lines of the ECal. The optimal voltage for each APD at 18 °C and a pre-selected gain of 150 can be extrapolated as shown in Fig. 3.4.10.

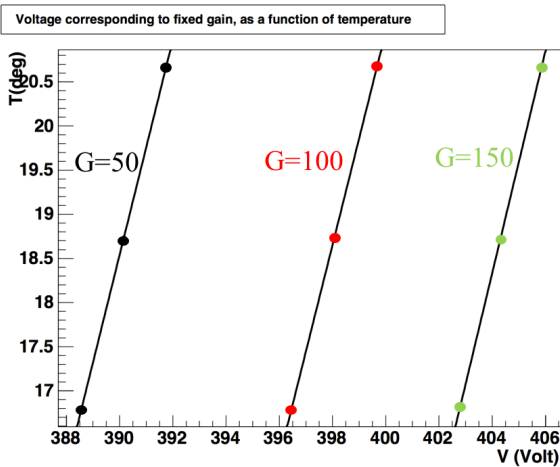


FIG. 3.4.10: The calculated voltages for fixed gains as a function of temperature can be used to group the APDs for common high voltage.

3.5 TRIGGER

Events of interest in the HPS experiment are triggered by the ECal. Each channel of the ECal is readout to an FADC250 with 16 channels per board. The FADC250 continuously samples analog signals at a rate of 250 MHz, or every 4 ns with 12-bit precision. As the data size was small enough, the 2015 and 2016 data was recorded in raw mode such that 100 samples of raw information in a channel are read at the trigger time. This raw mode, called Mode 1, allowed for precise offline pulse fitting of the signals for optimal energy resolution and improved timing resolution.

When a signal crosses a pre-defined threshold, a set number of samples before and after the crossing are summed together to provide a pulse charge value which is converted to energy. The conversion to energy requires access to the individual channel gains and pedestals (as found by cosmic calibrations) which are pre-loaded into the data acquisition (DAQ) system. The energy and time of threshold crossing are sent to the General Trigger Processor (GTP) board every 16 ns for clustering. [1]

The GTP clusterer first identifies the crystal carrying the highest energy (known as the seed hit) in comparison to all surrounding crystals. The immediately neighboring crystals of the seed hit are compared in both energy and time coincidence with respect to the seed crystal in order to create a cluster. The cluster energy is the sum of all of the hits in a cluster. The timing coincidence is typically chosen to be 4 samples to allow for time-walk effects. The cluster information is then passed to the Subsystem Processor (SSP) to make a trigger decision based on various settable trigger cut requirements.

The SSP includes several different configurations that can run simultaneously containing different settable cuts and prescale values for ECal modules. The SSP looks for combinations of clusters that pass the configuration requirements and cuts and then sends a trigger to the Trigger Supervisor (TS) board when a cluster or pair of clusters satisfies the trigger requirements. The trigger is then sent to the Trigger Interface (TI) boards in order to trigger readout of all detectors.

The SSP trigger configurations include two cluster pairs triggers, two single cluster triggers, a random pulser trigger, a cosmic trigger, and an LED trigger of which all except for the cosmic and LED trigger were run during data taking with beam. The single cluster trigger, Single-1, was optimized for elastically-scattered beam energy electrons off the target. The looser version of the trigger was Single-0. These triggers were useful in selecting events for calibrating the ECal and studying the trigger efficiencies. The cluster pairs trigger is the primary trigger for the HPS experiment and studies all possible combinations of clusters in the

ECal for pairs selection. The tuneable cuts used in this trigger are presented in Table 1. [1]

TABLE 1: Pair-1 Trigger Cuts

Trigger cut	Cut value
Time difference	$ t_{top} - t_{bot} \leq t_{coincidence}$
Cluster energy	$E_{min} < E_i < E_{max}$
Cluster sum	$E_{summin} \leq E_1 + E_2 \leq E_{summax}$
Cluster size	$N_{hits} \geq N_{threshold}$
Energy difference	$E_2 - E_1 < E_{difference}$
Coplanarity	$ \arctan \frac{x_1}{y_1} - \arctan \frac{x_2}{y_2} \leq \theta_{coplanarity}$
Energy-distance	$E_1 + r_1 F \geq E_{slope}$

In Table 1, the variables t_i, E_i, N_i, x_i , and y_i denote the cluster time, cluster energy, number of hits in the cluster, and coordinates of the cluster, respectively. The subscript, 1, denotes the cluster with the lowest energy of the pair. The parameter, r_1 , is the distance between the center of the lowest energy cluster and the center of the ECal (defined as $r_1 = \sqrt{x_1^2 + y_1^2}$). The parameters selected for the cuts include the $t_{coincidence}, E_{min}, E_{max}, E_{summin}, E_{summax}, N_{threshold}, E_{difference}, \theta_{coplanarity}, r_1$, and E_{slope} , and are chosen from studying A' Monte Carlo in order to optimize the signal acceptance while minimizing the background. The GTP clusters are created prior to track-matching and offline clustering (which includes hits belonging to a cluster beyond those immediately adjacent to the seed hit). For the 2015 data, a GTP cluster conserves roughly 80% of the fully reconstructed particle energy when the seed hit is not on the edge of the ECal.

The time coincidence cut is kept loose enough in the SSP pairs cluster selection to allow for time walk and cabling offsets which are not corrected for until the full pulse is fitted in offline reconstruction. At the GTP stage, the time only corresponds to threshold crossing. The cluster energy cut is inclusive of clusters that are reconstructed by the GTP in the energy range of interest. The minimum hit requirement for clusters was lowered at the start of running due to A' Monte Carlo studies indicating that 1 hit clusters were possible and could improve reach without overburdening the trigger. The cluster sum cut most significantly removes accidental pairs containing elastically-scattered beam energy electrons in addition to removing low energy cluster sum events that will not pass thresholds for well-reconstructed events. The energy difference cut removes events that have extremely different cluster energies and do not satisfy A'-type criteria.

The coplanarity cut removes events that are not coplanar including Møller and wide-angle bremsstrahlung (WAB) backgrounds because the $e + e -$ trident events of interest are distributed symmetrically around the beamline. The angle is calculated from the center of the ECal where the beam line passes through to each cluster in the pair relative to the vertical axis. The pairs should be approximately 180° apart.

The energy-distance cut is applied to the lowest-energy cluster of the pair in order to reject events where the cluster is too close to where the electron beam passes through the ECal. Trident kinematics show that most of these clusters are dominated by bremsstrahlung low energy photons and that there is some reasonable distance of separation with respect to the beamline for these lower energy events. The cut values used in the 2015 Pair-1 trigger are shown in Table 2.

TABLE 2: Pair-1 trigger cut values for the Engineering Run

Trigger cut	Cut value
Time difference	$ t_{top} - t_{bot} \leq 12$ ns
Cluster energy	$54 < E < 630$ MeV
Cluster size	$N_{hits} \geq 1$
Energy sum	$180 < E_{top} + E_{bot} < 860$ MeV
Energy difference	$ E_{top} - E_{bot} < 540$ MeV
Coplanarity	$\theta_{top} - \theta_{bot} < 30^\circ$
Energy-distance	$E_1 + (5.5\text{MeV/mm})r_1 > 600$ MeV

The pulser trigger generates a constant rate of triggers at 100 Hz regardless of the physics events as measured by the ECal. This makes the pulser an unbiased probe for measuring the backgrounds of the experiment during running with the beam and concurrent with other triggers.

The cosmic trigger was used without the beam for calibration of the ECal and uses the timing coincidence between two scintillators, placed below and external to the ECal, in order to trigger readout of all ECal channels for offline reconstruction of the cosmic event. The timing coincidence of the scintillators placed in line and below the ECal was chosen to be 40 ns where the leading edge of the scintillator signal in the FADC pulse crosses 60 ADC. Once the timing and threshold conditions are met, all modules in the ECal were readout in Mode 1 format.

CHAPTER 4

DETECTOR CALIBRATION AND PERFORMANCE

The first detector to be commissioned was the ECal during preliminary running with a 2 GeV electron beam in Hall B in December 2014. The ECal was initially calibrated prior to receiving any beam using cosmic ray energy deposition in the crystals. The ECal demonstrated that all channels worked and that the full readout chain using FADC250 modules with the DAQ performed well. The SVT was installed in the early spring of 2015 and was fully commissioned during the Engineering Run. The single pass beam energy was 1.056 GeV and was sufficient for detector commissioning, calibration, and physics analysis.

4.1 SILICON VERTEX TRACKER PERFORMANCE

The SVT momentum calibration is primarily guided by the accuracy of the alignment in the magnetic field. Tracks on both top and bottom for elastically-scattered electrons should peak at the same beam energy at the same resolution. The Billoir vertexing algorithm is the method by which two tracks are re-fit to create a vertex. The invariant mass is reconstructed from the vertex of the two tracks.

(Include discussion on layer efficiency, 3 prong tracking efficiencies, moller mass, and fee peak resolution.)

4.2 ELECTROMAGNETIC CALORIMETER

The ECal was calibrated both in energy and time. The first calibration performed before receiving beam from the accelerator was the cosmic ray energy calibration. A full timing calibration of the ECal was also performed using the accelerator RF signal. A final calibration using physics events from elastically-scattered beam energy electrons and events from wide angle bremsstrahlung (WAB) yielded the full calibration of the ECal for all energies and characterized the energy resolution.

4.2.1 SIMULATIONS

The ECal uses an adapted version of the clustering algorithm that was used by the CLAS IC. The geometrical arrangement of the crystals differs greatly from that used by the IC and

required detailed studies and simulations to reconstruct the incident particle energy. The angles of incidence of the particles (electrons, positrons, and photons) entering the ECal varies significantly across the ECal. The edge effects in the ECal are substantial due to the horizontal split between the top and bottom halves and the proximity to the beam.

Simulations were performed using the fully modeled detector geometry in SLIC as part of the standard hps software package. The geometry includes all strips of the SVT, vacuum chambers, ECal crystals, and relevant dead material. The geometry also moves particles through a 3D magnetic field map corresponding to the field values for 1 GeV beam running. [13]

Single particles: electrons, positrons, and photons were simulated at discrete energies of 0.2, 0.3, 0.4, 0.5, 0.6, 0.7, 0.8, 0.9, 1.0, and 1.1 GeV to uniformly cover the ranger of energies detectable in the Engineering Run. The simulation uses the full reconstruction chain excluding pile-up effects. The offline cluster reconstruction uses the same thresholds used in data and production Monte Carlo: 7.5 MeV for individual hits, 50 MeV for seed hits in clusters, and 100 MeV for cluster energies.

Energy reconstruction

Due to the complex showering cascade that occurs when a particle deposits its energy in the ECal, several adjacent crystal modules contain some fraction of the incident energy of the particle. These modules are clustered in offline reconstruction to obtain the total deposited energy of the incident particle. The reconstructed energy not corrected for shower loss effects is defined by Equation (4.2.1).

$$E_{rec} = \sum_i E_i \quad (4.2.1)$$

In Equation (4.2.1), the subscript i pertains to each module in the cluster such that E_i is the energy of each module in the cluster. Some incident particle energy is lost between crystals and out the back where the APD does not fully cover the surface of each crystal. After recovering the energy as measured by the ECal, the incident particle energy can be found by correcting for the shower loss effects as described by Equation (4.2.2).

$$E_{corr} = \frac{E_{rec}}{f} \quad (4.2.2)$$

In Equation (4.2.2), f is the energy-dependent ratio of measured vs incident particle

energy. This factor is obtained through simulation. The energy loss corrections as derived from Monte Carlo are shown in Fig. 4.2.1 where E_{gen} refers to the simulated Monte Carlo particle energy.

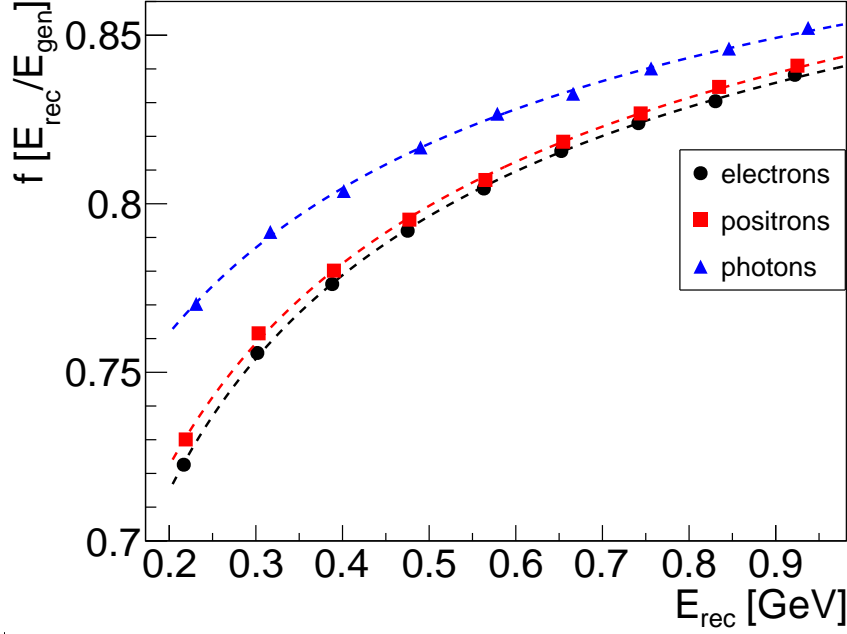


FIG. 4.2.1: Energy correction functions correct the energy measured in the ECal to reconstruct the energy of the incident particle.

The difference in the energy corrections for the various particle types arises from geometrical effects and the incident angles of the particles entering the crystals. [3] The focal point of the calorimeter, the point at which all crystals are angled, lies 80 cm from the front face of the ECal. The HPS target is beyond this focal distance at approximately 1.3 m from the face of the ECal and is offset beam right in the pair spectrometer magnetic field. Particles produced at the target take different trajectories from the target to the ECal due to the interactions of their charge and momentum in the magnetic field. This affects the entry angle of the particle into a crystal and mandates a charge and momentum-dependent energy correction function. The form of the energy correction function for the central region of the ECal is described by a three parameter fit in Eq. (4.2.3).

$$\frac{E_{rec}}{E_{gen}} = \frac{A}{E_{rec}} + \frac{B}{\sqrt{E_{rec}}} + C \quad (4.2.3)$$

The shower leakage effects in crystals becomes significant at distances close to the edge. The energy reconstruction deteriorates rapidly in the crystals closest to the edge but stabilizes

in central region of the ECal. The energy reconstruction at the edges was fully characterized using Monte Carlo as a function of position in the ECal relative to the inner beam gap edge. In Equation (4.2.3), parameter A is not strongly correlated with position and remains as a constant for a given particle type. The parameters B and C do depend on cluster position relative to the beam gap edge of the ECal. These dependencies can be seen for electrons in Fig. 4.2.2.

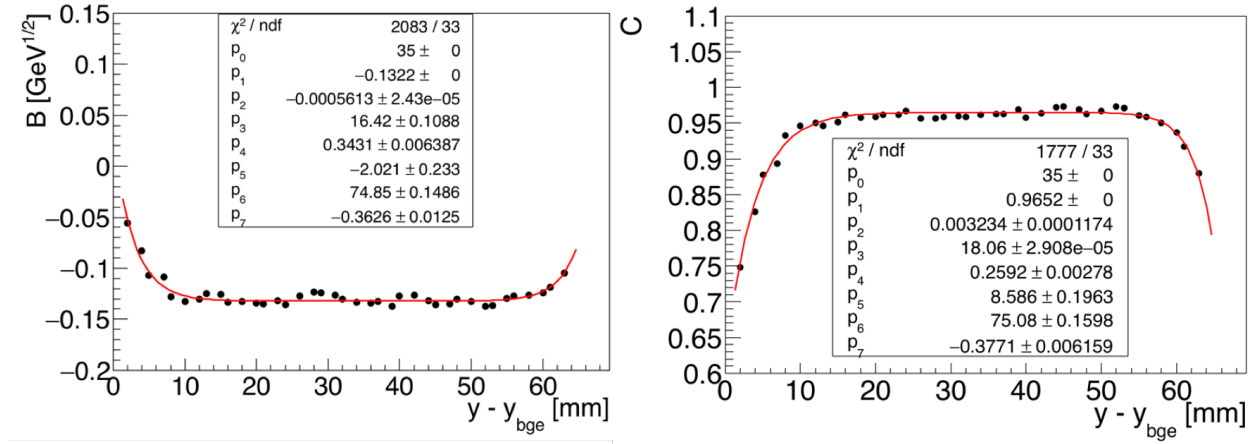


FIG. 4.2.2: Parameters B and C from Eq. 4.2.3 for electrons, as a function of vertical position relative to the innermost beam gap edge.

As shown in Fig. 4.2.2, the energy leakage parameters B and C can be fit with two functions at the edges that match in the central region of the ECal, away from the edges of the calorimeter. The equations used to fit the B and C parameters are described by Equations (4.2.4) and (4.2.5), respectively.

$$\begin{aligned} B(y < p_0) &= p_1 - p_2 e^{-(y-p_3)p_4} \\ B(y > p_0) &= p_1 - p_5 e^{-(y-p_6)p_7} \end{aligned} \quad (4.2.4)$$

$$\begin{aligned} C(y < p_0) &= p_1 - p_2 e^{-(y-p_3)p_4} \\ C(y > p_0) &= p_1 - p_5 e^{-(y-p_6)p_7} \end{aligned} \quad (4.2.5)$$

The energy leakage correction functions are relatively constant in the central region of the calorimeter and are matched at a central distance p_0 . For columns containing 5 crystals vertically, the distance to the beam gap edge is the absolute value of the distance from the cluster centroid to the innermost beam gap edge. In the regions above and below the

region where row 1 crystals are removed in the ECal, additional consideration is made when calculating the distance to the inner beam gap edge in order to be consistent with other regions of the ECal. For completeness, the corresponding energy correction parameters for positrons and photons are seen in Figures 4.2.3 and 4.2.4, respectively.

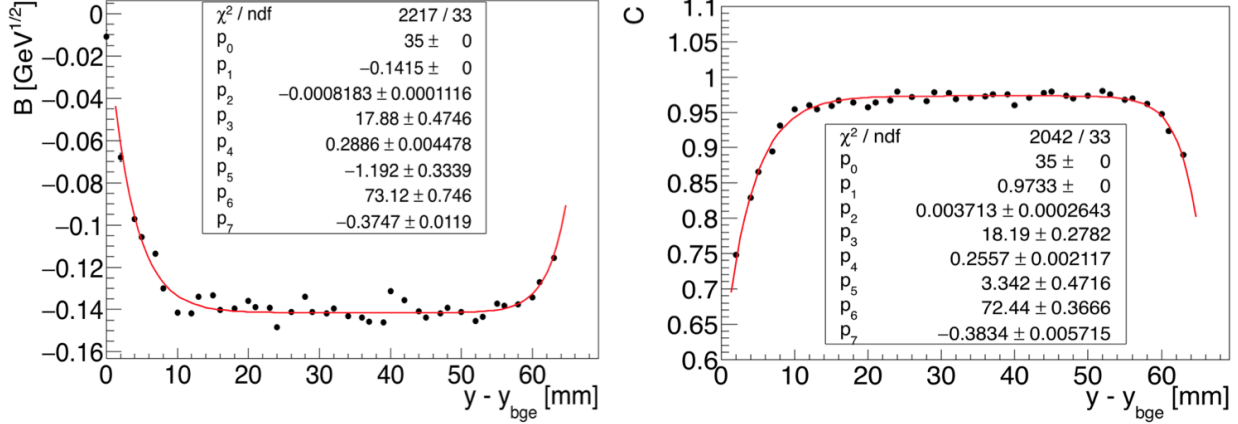


FIG. 4.2.3: Parameters B and C from Eq. 4.2.3 for positrons, as a function of vertical position relative to the innermost beam gap edge.

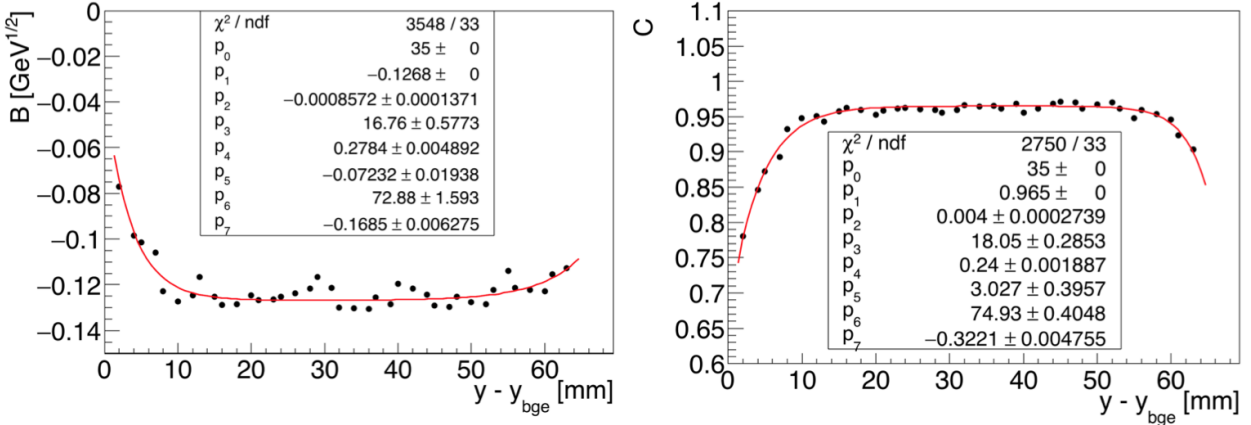


FIG. 4.2.4: Parameters B and C from Eq. 4.2.3 for photons, as a function of vertical position relative to the innermost beam gap edge.

As one can see, the energy corrections are relatively constant at approximately 1 cm from the edges of the ECal. As a result, we define the fiducial the region of the ECal to be at greater than 1 cm from the edge, or approximately 3/4 of the font face crystal dimension. This result is consistent with the findings for the CLAS IC. [3]

Energy resolution

The energy resolution of the ECal is energy-dependent and improves with energy as $1/\sqrt{E}$. From simulation, we obtain the energy resolution as shown in Figure 4.2.5.

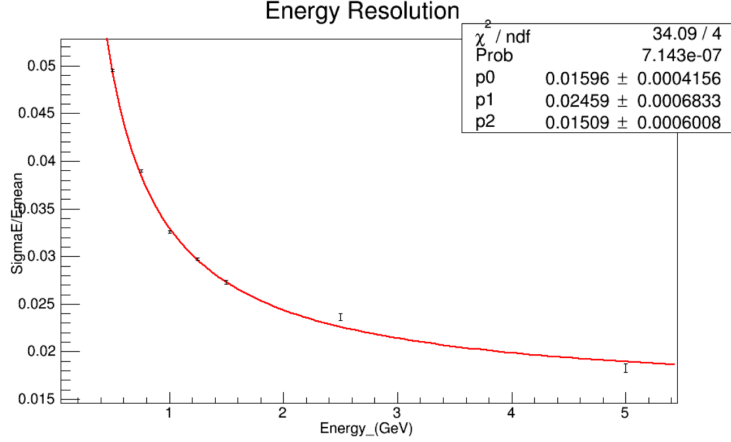


FIG. 4.2.5: ECal energy resolution from simulation.

The fit shown in Figure 4.2.5 is described by Equation 4.2.6.

$$\frac{\sigma_E}{E} (\%) = \frac{1.60}{E} \oplus \frac{2.46}{\sqrt{E}} \oplus 1.51 \quad (4.2.6)$$

The first term corresponds to the preamplifier noise. We were expecting $3 \text{ MeV} \times \sqrt{10} = 0.009 \text{ GeV}$, where 10 is the average number of hit crystals. This term from simulation is not including the FADC error (expected to be 1.3 MeV [10]) which contributes a term (in %) as $0.13\sqrt{10}/E$ to be added, quadratically. The second term corresponds to the statistical fluctuations in the shower development and is influenced by the lateral containment of the shower and energy deposited in the crystal module. The second term from simulation is not including fluctuations in the number of photoelectrons (30 photoelectrons/MeV, multiplied by an excess noise factor parameterizing the fluctuations in the APD gain process, or Fano factor, of 2 [16]) contributing $0.8/\sqrt{E}$. This term is calculated as $\sqrt{F/N_{pe}/GeV}$. The third term is interpreted as the fluctuation of energy leakage through the back of the crystals. This third term should include the crystal-to crystal inter-calibration error which estimate to be 1 %. [3] By including these additional resolution effects in the measurement, we obtain the resolution as anticipated from Monte Carlo in Equation (4.2.7).

$$\frac{\sigma_E}{E} (\%) = \frac{1.65}{E} \oplus \frac{2.59}{\sqrt{E}} \oplus 1.81 \quad (4.2.7)$$

Position reconstruction

ECal clusters provide position information of comparable resolution to the SVT. Various weighting schemes for calculating a cluster centroid can be problematic due to periodic patterns resulting from the segmentation of the crystals. The same weighting scheme, used by the CLAS IC algorithm, provided the optimal position resolution. The calculation of the position of the cluster is shown in Equation (4.2.8). [3]

$$\begin{aligned} x_{cl} &= \frac{\sum_i w_i x_i}{\sum_i w_i} \\ y_{cl} &= \frac{\sum_i w_i y_i}{\sum_i w_i} \end{aligned}$$

In Equation (4.2.8), the index i indicates the individual module in the cluster, and w_i is described by Equation (4.2.8).

$$w_i = \max[0, w_0 + \ln \frac{E_i}{E_{rec}}] \quad (4.2.8)$$

The parameter w_0 in Equation (4.2.8) is an energy threshold such that $E_i/E_{cl} > e^{-w_0}$ and is found in simulation to have a value of 3.1 [3]. The logarithmic term enhances the contribution from the tails and improves the position measurement. Additional effects resulting from the differing angles of entry at the ECal require a position correction to the x -coordinate of the cluster. These corrections are both charge and momentum-dependent. The position correction for a generated 1 GeV electron is shown in Figure 4.2.6.

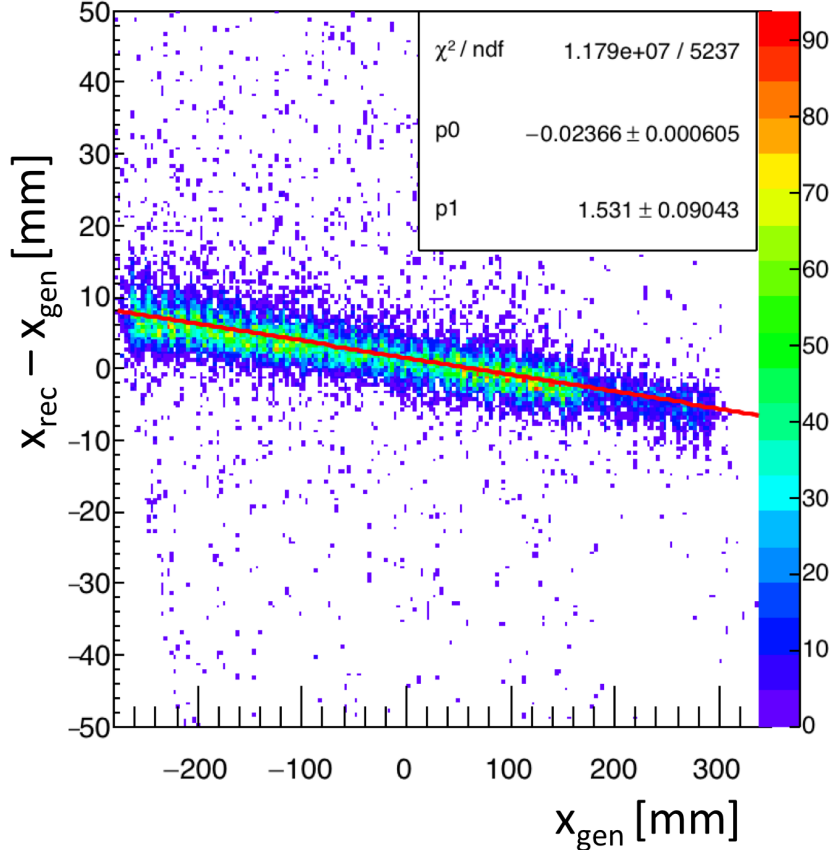


FIG. 4.2.6: The position correction as found for a 1 GeV electron is both energy and position-dependent in order to account for the different angle of incidence at the ECal.

The correction at each energy by particle-type is fit with Equation (4.2.9).

$$x_{rec} - x_{gen} = A(E_{rec})x_{gen} + B(E_{rec}) \quad (4.2.9)$$

The energy-dependence of the fit parameters $A(E_{rec})$ and $B(E_{rec})$ use the reconstructed cluster energy, uncorrected for shower loss effects. These parameters for the electron horizontal position correction as a function of the reconstructed cluster energy are shown Figure 4.2.7.

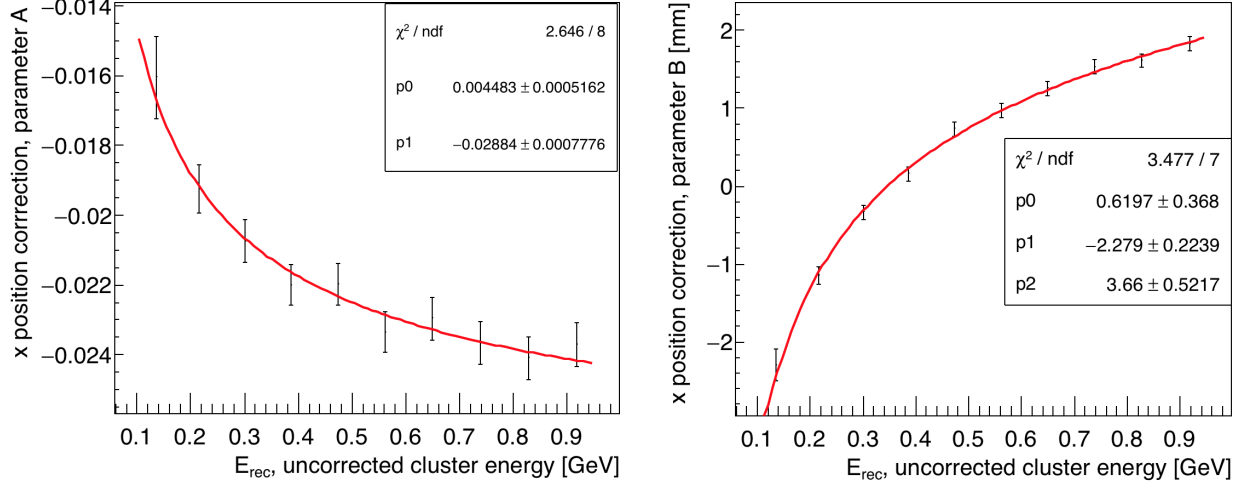


FIG. 4.2.7: The horizontal position correction parameters as functions of the uncorrected cluster energy.

The parameters in Figure 4.2.7 are fit to functions of the form described in Equation (4.2.10).

$$\begin{aligned} A(E_{rec}) &= \frac{p_0}{\sqrt{E_{rec}}} + p_1 \\ B(E_{rec}) &= p_0 \times E_{rec} + \frac{p_1}{\sqrt{E_{rec}}} + p_2 \end{aligned}$$

The corresponding correction values for all three particle types can be summarized in Table 3.

TABLE 3: Horizontal position corrections.

Particle	$A(E_{rec})$	$B(E_{rec})$
electron	$0.004483/\sqrt{E_{rec}} - 0.02884$	$0.6197E_{rec} - 2.279/\sqrt{E_{rec}} + 3.66$
positron	$0.006887/\sqrt{E_{rec}} - 0.03207$	$-0.8048E_{rec} + 0.9366/\sqrt{E_{rec}} + 2.628$
photon	$0.005385/\sqrt{E_{rec}} - 0.03562$	$-0.1948E_{rec} - 0.7991/\sqrt{E_{rec}} + 3.797$

Position corrections are not needed for the vertical cluster position.

Position resolution

After applying the position corrections to each particle-type at the simulated energies, the residual between the measured and simulated position reconstruction is obtained is measured.

The fitted residuals after correcting the position of 1 GeV electron clusters are shown in Figure 4.2.8.

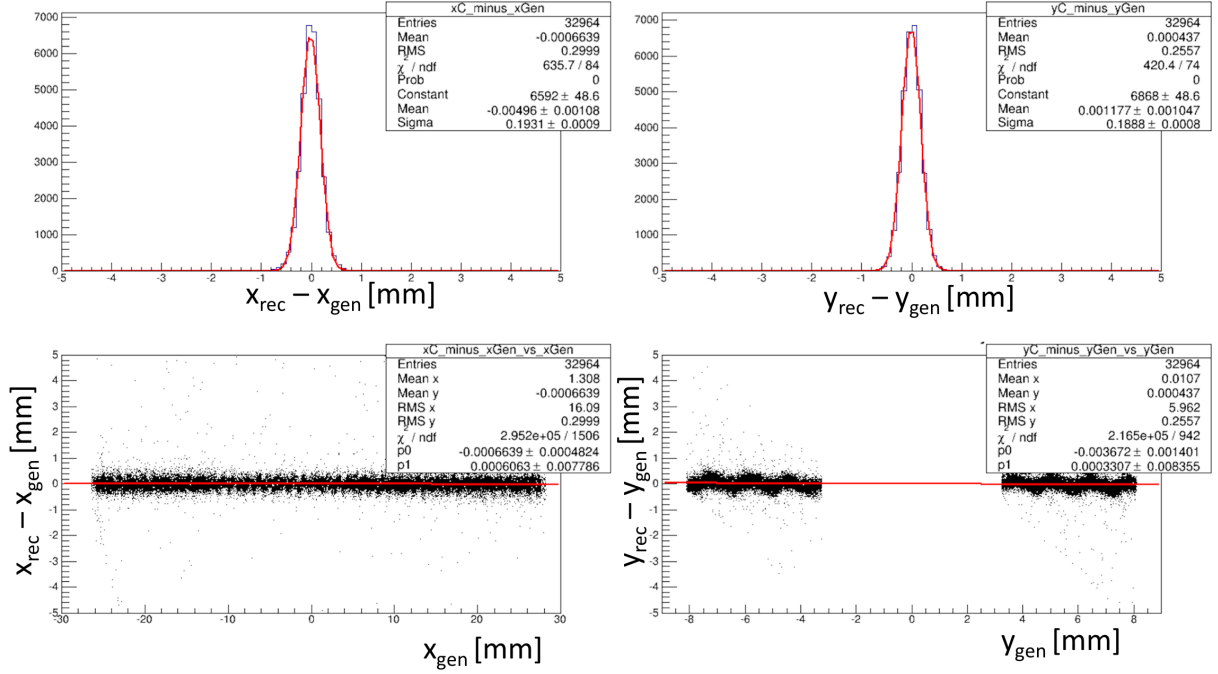


FIG. 4.2.8: The position resolution for 1 GeV electrons, after applying the horizontal position corrections.

As shown in Figure 4.2.8, no correction is required when reconstructing the vertical position of the cluster. The energy-dependent resolution of both the horizontal and vertical position of reconstructed clusters can be seen for electrons in Figure 4.2.9.

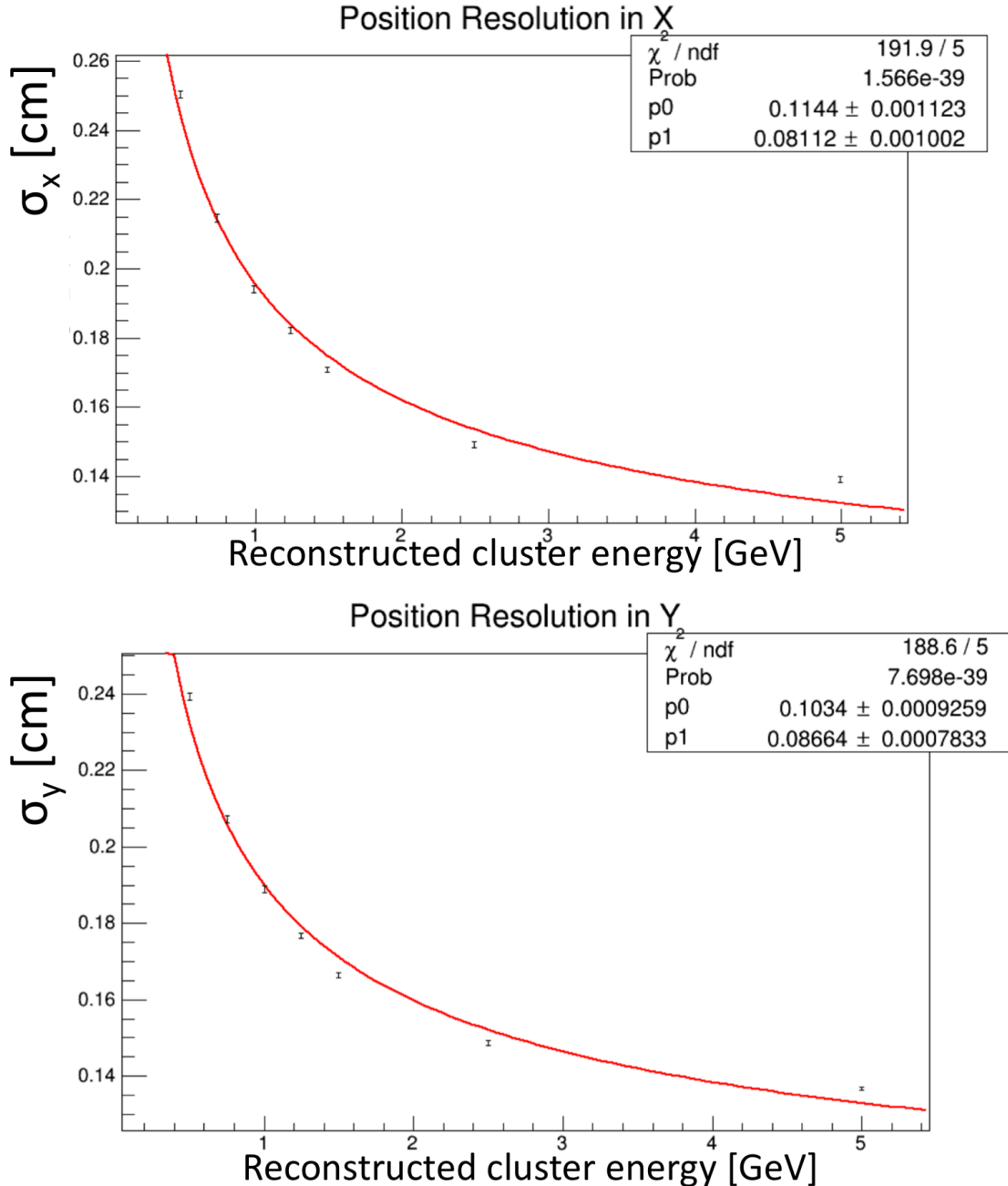


FIG. 4.2.9: The energy-dependence of the position resolution for electrons.

The position resolution is parameterized in terms energy following Equation (4.2.10).

$$\begin{aligned}\sigma_x &= \frac{p0_x}{\sqrt{E}} + p1_x \\ \sigma_y &= \frac{p0_y}{\sqrt{E}} + p1_y\end{aligned}$$

The parameters $p0$ and $p1$ are found by fitting the residuals for the energies. The position resolution is better than 2 mm for 1 GeV electrons. As the ECal face is located at approximately 1.4 m from the target, the ECal provides valuable position information when matched with a track. The position resolution for all particle types in the ECal is summarized in Table 4.

TABLE 4: Position resolution.

Particle	σ_x [mm]	σ_y [mm]
electron	$0.1144/\sqrt{E_{rec}} + 0.08112$	$0.1034/\sqrt{E_{rec}} + 0.08664$
positron	$0.1268/\sqrt{E_{rec}} + 0.07711$	$0.1068/\sqrt{E_{rec}} + 0.08423$
photon	$0.1255/\sqrt{E_{rec}} + 0.08877$	$0.1005/\sqrt{E_{rec}} + 0.08867$

4.2.2 CALIBRATION USING COSMIC RAY ENERGY

The large area APDs enabled the ECal to have the sensitivity to detect signals from cosmic muons traversing the ECal crystals perpendicularly. This signal was used for the initial calibration of the modules. The experimental setup was modeled using Monte Carlo simulations so that the energy deposited in the crystals from cosmic ray muons and rates could be studied. By measuring the average path length of cosmic ray muons in each crystal, the energy deposited in each crystal of the ECal was calculated using the known energy deposition from 2 GeV muons [9].

The experimental setup for the cosmic calibrations used two scintillators placed below the ECal to trigger readout of all of the crystals. A schematic for the setup of the cosmic calibration is shown in Fig. 4.2.10.

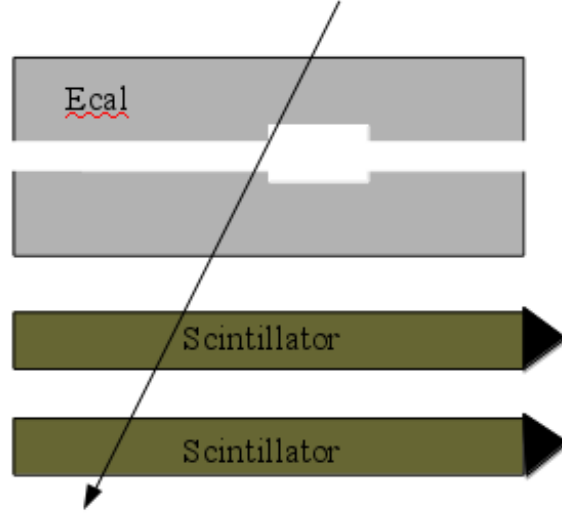


FIG. 4.2.10: Experimental setup for the cosmic ray calibration. As a cosmic ray passes vertically through both scintillators, event readout is triggered.

Each scintillator measures 75 cm long, 22 cm wide and 5 cm thick covering a slightly larger perpendicular area than the ECal crystals. The two scintillators are less than half a meter apart with the closest scintillator less than half a meter beneath the ECal. The energy deposited in each crystal in a layer is sensitive to the path length of the track as it passed through the crystal. From simulation, the average energy deposited in a crystal by a cosmic ray passing vertically through the ECal is shown in Fig. 4.2.11.

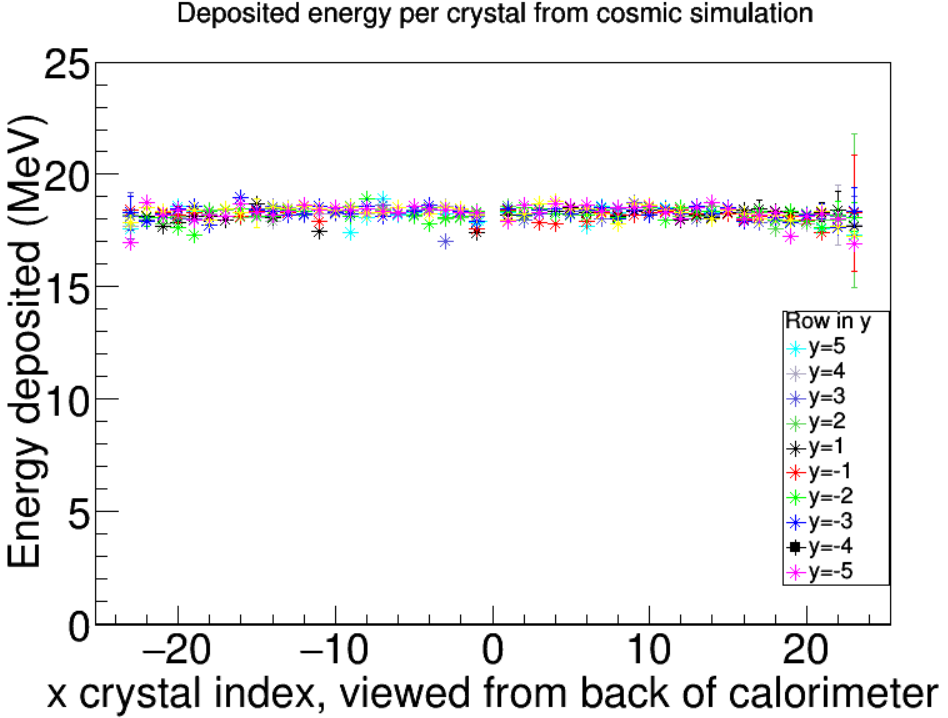


FIG. 4.2.11: The simulated cosmic ray muon energy deposition per crystal of the ECal. The mean energy was 18.3 MeV.

In Fig. 4.2.11, only tracks passing through one crystal in a row were included. Additionally, the cosmic ray muon track had to pass through an adjacent crystal in the row above and below a crystal. For crystals near edges, the geometrical requirement was adjusted to include the two crystals immediately above (or below for cases where the edge is above the crystal) the crystal being readout. The average energy deposited per crystal is approximately 18.3 MeV from the PDG.

In data, the raw FADC waveform for each crystal is readout, and the event is kept for further study after applying strict coincidence cuts between the two scintillators. The trigger rate for data is about 7 Hz. 30% of events passed the coincidence cut between the scintillators. For a track passing vertically through all ten layers, we can see the signal in each crystal as shown in Fig. 4.2.12.

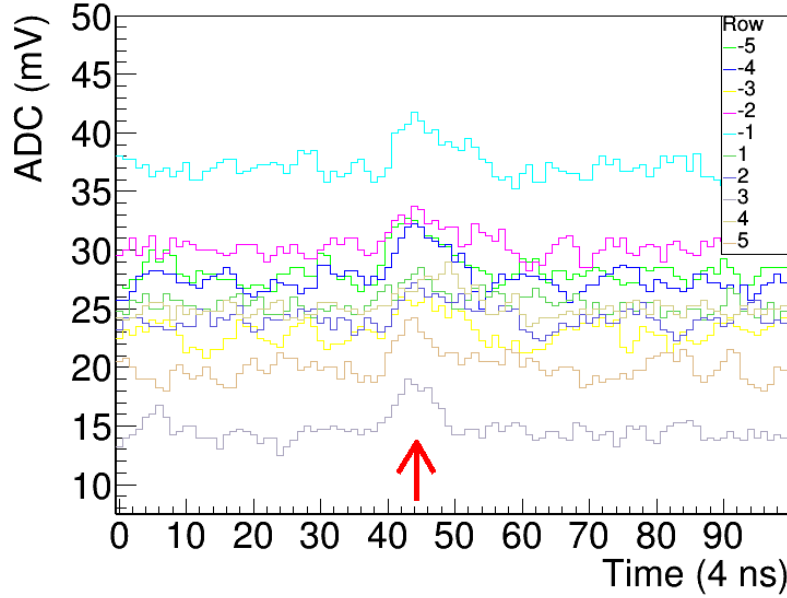


FIG. 4.2.12: Cosmic ray signal passing vertically through all ten layers of crystals in the ECal. Each crystal’s signal is separated vertically in this plot by its pedestal. The arrow indicates the approximate place in time that the cosmic signal passed through the detector.

As seen in Fig. 4.2.12, each FADC channel has a unique pedestal value. The pedestal for each event was calculated as an average of the first twenty bins of the time window. By searching for a threshold crossing in the time window where cosmic events occurred, the signal was then fully integrated and the pedestal was subtracted. The raw waveform thresholds were 2.5 mV in 2015 and increased to 3.5 mV in 2016 to accommodate the larger signals after the removal of the splitters. Geometric cuts are then applied to the data in offline analysis. Crystals having peaks over a certain threshold must have at least an adjacent crystals located above and below with threshold crossing, but the crystals to the left and right must not cross threshold. These cuts ensure that the track passed as vertically as possible through the ECal (reducing the variations in path length across each crystal). The integrated signals over many events in each crystal were fit. An individual crystal fit is shown in Fig. 4.2.13.

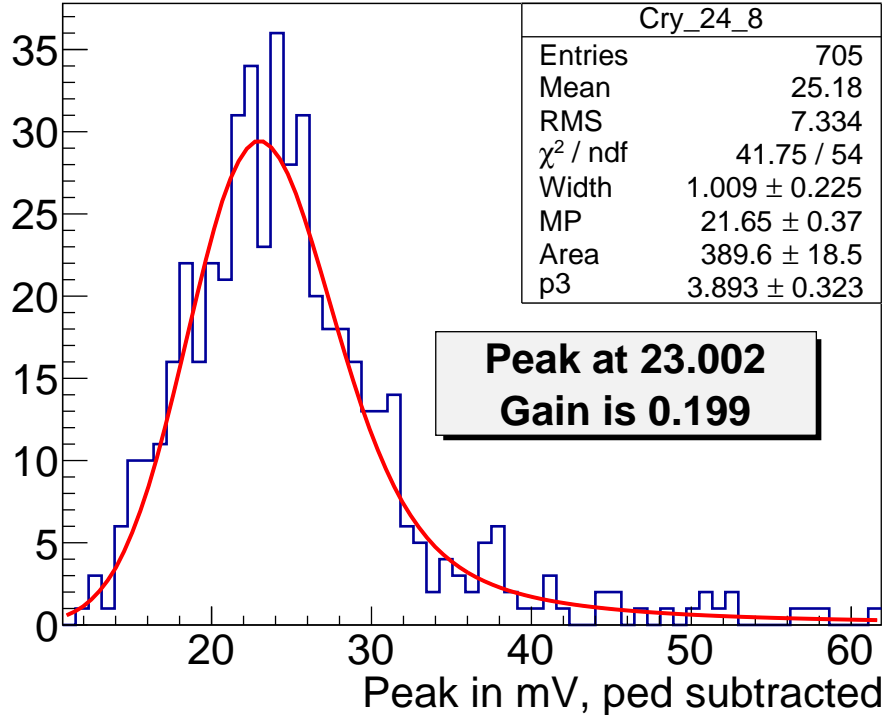


FIG. 4.2.13: Each cosmic signal was integrated and then fit using a Landau-Gaussian convolution function. The peak was calculated numerically from this fit.

The fit shown in Fig. 4.2.13 utilized a Landau-Gaussian convolution as the Landau part corresponds to the crystal's response to a particle's energy deposition as ionization energy loss, and the Gaussian part accounts for the statistical nature of the electronics shaping and readout. The peak of the fit is calculated numerically, and the initial conversion from units of FADC to energy (MeV) is obtained (called the Gain factor). The unit conversion from units mV to FADC is 1 V to 4096 FADC. The 4096 FADC counts can be set to 1 V or 2 V, but for 2015 and 2016 running, the setting was 1 V. This arises from the 12 bit conversion which yields 4096 FADC. The gain factor is calculated using the measured peak position in units of FADC and the known energy deposited from simulation in units of MeV as shown in Eqn. (4.2.10).

$$\text{Gain} = \frac{[\text{MeV}]}{[\text{FADC}]} \quad (4.2.10)$$

After approximately 60 hours of cosmic data, the full ECal could be calibrated using cosmics, and the resultant gains for all channels in the Engineering Run is shown in Fig. 4.2.14 and Fig. 4.2.15.

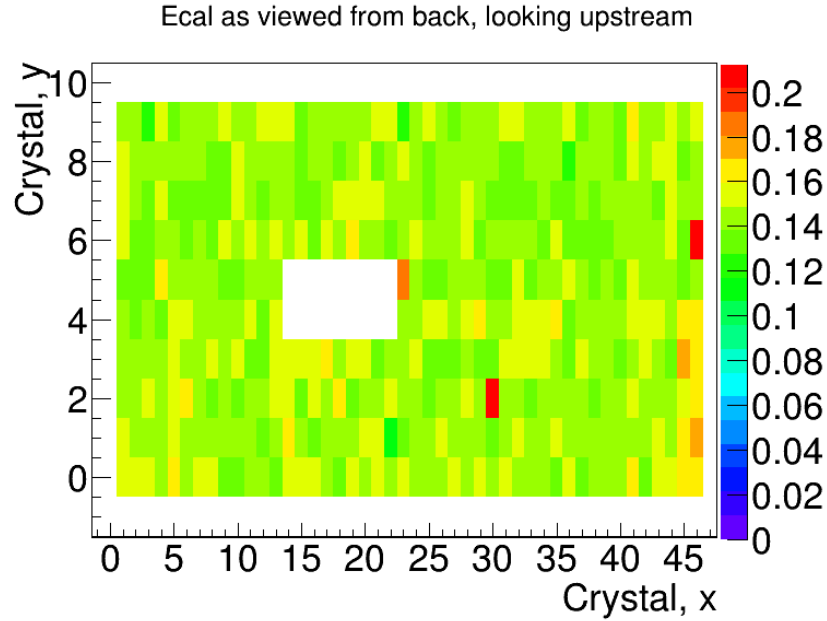


FIG. 4.2.14: Resulting gain calibration using cosmics for the Engineering Run.

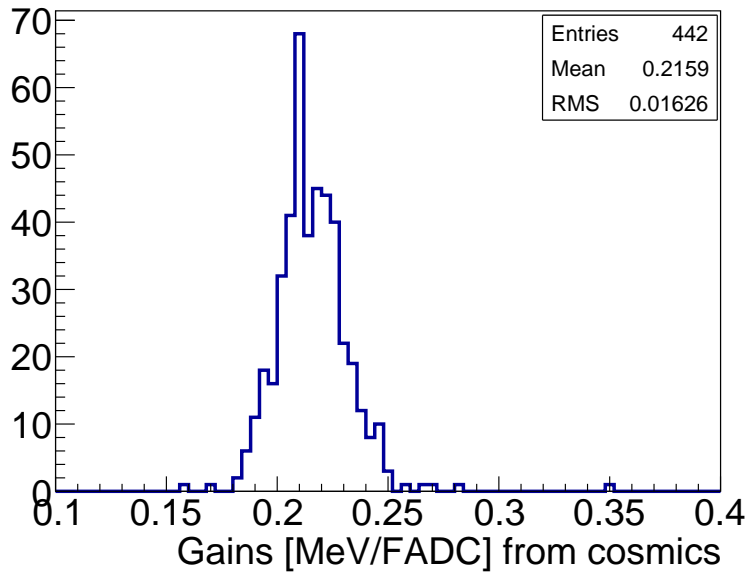


FIG. 4.2.15: Resulting gain calibration using cosmics for the Engineering Run.

With the splitters installed in the ECal readout chain, the average gain value was around 0.2 MeV/FADC for the Engineering Run. After the removal of the splitters in January 2016, prior to the Physics Run, the average gains were found to be around 0.13 MeV/FADC.

4.2.3 ECAL SIGNAL PULSE FITTING

All data was taken using the FADC250 modules which sample at 250 MHz, or every 4 ns. While the firmware has various modes capable of recording data, size was not an issue and Mode 1 was used during the Engineering and Physics Runs. Mode 1 preserve the full measured waveform for a module hit and improved methods for extracting the energy and time information from a hit can be done in offline analysis. The trigger decision to readout a module is based off a leading edge threshold which was set to 12 FADC units in the Engineering Run.

The full readout response for each module was carefully studied in order to understand the time response and shaping effects of the preamplifier on the ECal modules [10]. It was found that the raw waveform response was best described by the sum of the pedestal P and a $3-pole$ function for the pulse with width τ and occurring at time t_0 as shown in Eq. (4.2.11) [10].

$$P + \frac{A}{2\tau^3}(t - t_0)^2 e^{-(t-t_0)/\tau} \quad (4.2.11)$$

The pulse integral value is parameter A . When $t < t_0$, the pulse amplitude is zero. The best resolutions were found by fixing the width parameter for each module as an average of width module as measured over several pulses. An example fit is shown in Fig. 4.2.16.

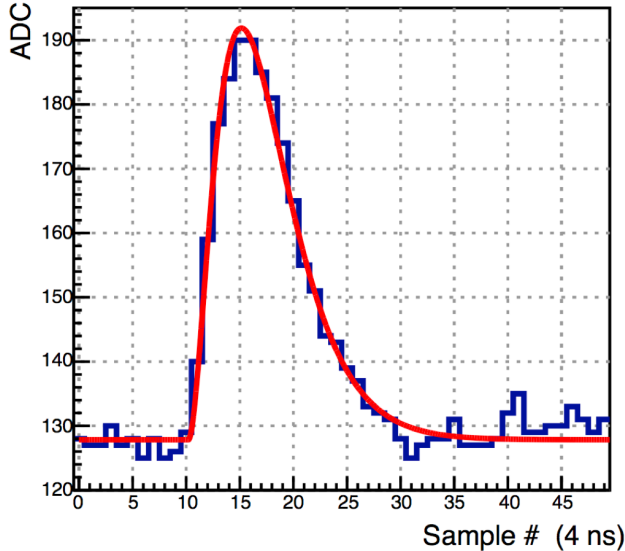


FIG. 4.2.16: Example fit to a real ECal module pulse.

The pedestal is calculated event-by-event and initialized by a running average over the

previous fits for the pulse. The fit range was set to 20 ns before threshold crossing and 60 ns after in order to eliminate contamination from pile-up signals in the same event [11]. The pulse-fitting of the raw waveform demonstrated the best time resolution and energy resolution when compared to the other hardware integral methods that could have been implemented [11].

4.2.4 CALIBRATION USING ELASTICALLY-SCATTERED ELECTRONS

The calibration using cosmic ray muons was sufficient for initial data-taking with the electron beam, but the overall energy calibration of the ECal is optimal at higher energies. The ECal detects electrons from elastic scattering at the target that peak, after correction for shower leakage effects, at the beam energy. As the target is off centerline beam right, there are geometric effects that prevent elastically-scattered beam energy electrons from full coverage of the ECal. [13] From simulation, the first column of crystals on beam right, and the five columns of crystals on beam left cannot be calibrated using elastically-scattered electrons.

To calibrate the ECal using elastically-scattered electrons, we selected events where the seed hit crystal carried at least 60% of the overall cluster energy. The seed hit was also required to have carried greater than 450 MeV in the 2015 data (1.1 GeV for the 2016 dataset), to have triggered a Singles-1 event readout from the DAQ, and to have occurred in the optimal trigger timing window. The cluster energy was associated with the seed hit module for the calibration. The calibration uses an iterative procedure, by which the reconstructed peak energy is matched to that found by simulation (prior to energy corrections). For each peak, an iteration coefficient is found that reflects the ratio of the peak position measured in Monte Carlo to the peak position found for a particular iteration in the data. This ratio can be seen in Equation (4.2.12).

$$C_i = \frac{MC_{peak}}{data_{peak}} \quad (4.2.12)$$

After each iteration, this ratio C_i is applied to the original gain coefficient as well as any coefficient found from previous iteration. The data is re-processed applying these changes to the gains and clustering is re-run. This procedure continues until the correction coefficients found in a particular iteration are all less than 1%. Crystals on the edge of acceptance with poorly resolved peaks were given an iteration coefficient of 1. After completion of the calibration (approximately 2-3 iterations) [13], the shower loss correction functions were applied to the reconstructed cluster energies. The final peak position for

elastically-scattered electron clusters in the fiducial region of the ECal is shown in Figure

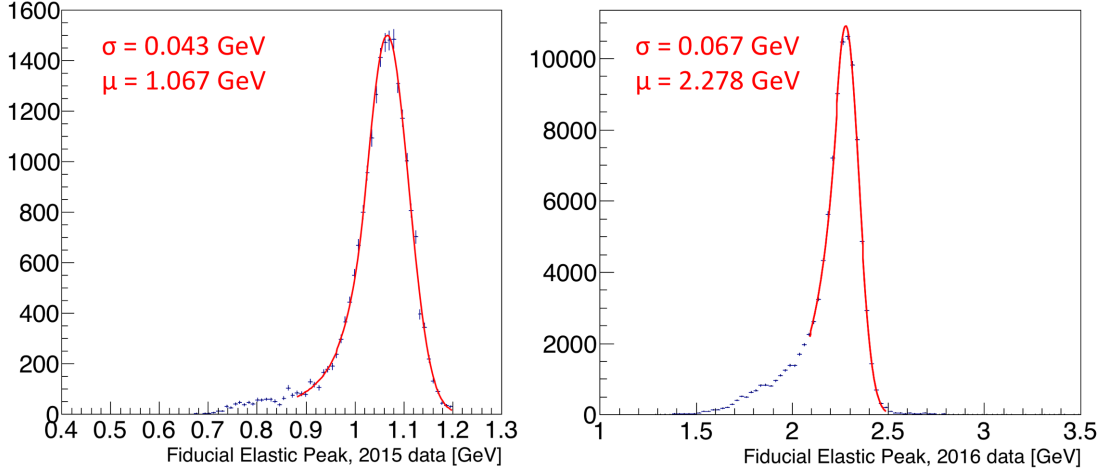


FIG. 4.2.17: Shown are the resultant fiducial peaks for the Engineering and Physics Runs on the left and right, respectively. The peaks are fit with a Crystal Ball function and the peak position and widths are indicated.

The energy resolution improves with the beam energy. The cluster energy spectrum is fit with a Crystal Ball function which contains a Gaussian component and a power law low energy tail. The ECal has an energy resolution of approximately 4% in the fiducial region at approximately 1 GeV and 2.9% at 2.3 GeV.

The final gains obtained after calibration with elastically-scattered electrons were compared to the gains obtained with cosmics alone in order to check for systematic offsets. While no systematic offsets were found, the comparison between the low and high energy calibrations tells us that the initial energies used for the cosmic calibration are roughly accurate, but it is limited in telling us anything about the linearity of the gain between these two energies. [13] If there was found to be any systematic offsets, these should be applied to the gains of the crystals that could not be calibrated using the elastically-scattered electrons due to acceptance, and the effects on the triggered data would need to be quantified.

4.2.5 WIDE ANGLE BREMSSTRAHLUNG FOR STUDIES OF EDGE EFFECTS

The primary physics trigger looks for two cluster events and recorded a high yield of WAB particles composed of a final state electron and photon. The spectrum of cluster energies in the Engineering Run dataset shows an excess of WAB events occurring where the energy

sum of the two particles is approximately equal to the uncorrected beam energy.

Initial studies after the calibration using elastic electrons showed that the energy sum of two particles in WAB events having mid-range energies was lower than the reconstructed elastic energy, indicating that the shower loss corrections in the mid-range beam energy required further investigation. WAB events were used to refine the shower loss corrections for mid-range energy particles. WAB events are identified by have track-matched clusters and no track matching a photon cluster. The reconstructed energy sum of the two particles must be equivalent the beam energy as shown in Equation (4.2.13). [13]

$$E_i = \frac{E_{e-}}{f_{e-}(E_{e-})} + \frac{E_\gamma}{f_\gamma(E_\gamma)} \quad (4.2.13)$$

In Equations (4.2.13) and (4.2.15), f refers to the shower loss correction described by Equation (4.2.2). The underlying assumption is that the relationship between the electron and photon shower loss corrections found in Monte Carlo are preserved according to Equation (4.2.14).

$$\frac{f_{e-,data}(E_{e-})}{f_{\gamma,data}(E_\gamma)} = \frac{f_{e-,MC}(E_{e-})}{f_{\gamma,MC}(E_\gamma)} \quad (4.2.14)$$

In maintaining the relationships shown in Equations (4.2.13) and (4.2.14), a chi-squared minimization yields the optimal adjustments to the shower loss correction functions for mid-range energy particles as shown in Equation (4.2.15).

$$\chi^2 = \sum_i \frac{(E_{beam} - E_i)^2}{\sigma_{e-}^2(E_{e-}) + \sigma_\gamma^2(E_\gamma)} \quad (4.2.15)$$

For each event, the energy sum of the two corrected clusters, E_i , is calculated as described by Equation (4.2.15). The end result is a small correction to the shower loss correction functions that ranges across the cluster energies and never exceeds a difference of 2%. [13] After incorporating these updated corrections to the shower loss correction functions, the energy resolution can be extracted for all energies and positions in the ECal.

4.2.6 ENERGY RESOLUTION IN DATA

The elastically-scattered electrons provided the clearest point in extracting the energy resolution of the ECal at the beam energy. Using WAB particles, electrons and photons, the energy resolution of the ECal was fully characterized in terms of energy and position relative to the edges.

To study the energy resolution in the fiducial region of the ECal, all electrons were matched to tracks, and the track position extrapolation to the face of the ECal was used to determine the electron's vertical distance relative to the beam gap edge. For WAB electrons, the photon cluster was required to be at least 10 mm from the ECal edges to avoid edge effects. By selecting WAB events where the energy difference between the two particles is less than 100 MeV, the resolution of the energy sum peak was fitted to extract the resolution. The resolution was extracted according to Equation (4.2.16).

$$\sigma_{E_\gamma + E_{e^-}}^2 = \sigma_{e^-}^2(E_{e^-}) + \sigma_\gamma^2(E_\gamma) \quad (4.2.16)$$

When both particles are in the fiducial region and are roughly equal in energy, then the energy resolution of the sum could be divided by $\sqrt{2}$ assuming that the energy resolution of both particles is the same. This same procedure was used to study the resolution when the particle energies were more asymmetric in energy in order to obtain the single particle energy resolution at various energies.

The experimentally-obtained fiducial energy resolution agrees well with Monte Carlo but generally yields a larger energy resolution across all energies (on the order of about 15%). The energy resolution obtained in data is shown in Figure 4.2.18.

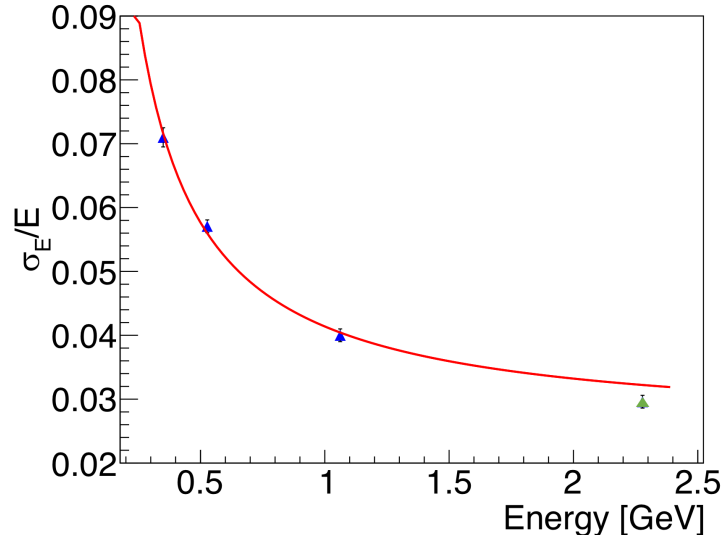


FIG. 4.2.18: The blue points are derived from the Engineering Run for the energy resolution of a single particle. The green point at approximately 2.3 GeV was determined from the elastic calibration of the Physics Run data. The fitted energy resolution was determined from the Engineering Run data only, but it is shown here extrapolated to higher energies.

The fit to the energy resolution in data is shown in Equation (4.2.17) and uses the blue points from the Engineering Run data in Figure 4.2.18.

$$\frac{\sigma_E}{E}(\%) = \frac{1.62}{E} \oplus \frac{2.87}{\sqrt{E}} \oplus 2.5 \quad (4.2.17)$$

The first term in Equation (4.2.17) is attributed to the noise from the pre-amplifiers and is roughly consistent to that found in Monte Carlo. The second term is related to the statistical fluctuations of the shower containment and the APD gain. This term is larger than the term found in Monte Carlo but is still consistent. The third term contains both the energy leakage out the back of the ECal as well as the crystal-to-crystal inter-calibration error. This term is significantly higher than anticipated from Monte Carlo, but is comparable to that found for the IC. It's possible that this term is affected by the inability to calibrate several crystals along the outer edges of the calorimeter with elastics.

The energy resolution from the Physics Run (shown in green on Figure 4.2.18) is slightly better than that predicted by the fit from the Engineering Run. It is likely that the energy resolution of the ECal improved overall because the signal going into the FADC modules was no longer split with TDC modules.

The WAB events were additionally a useful tool for studying the energy resolution in the ECal as a function of position relative to the edge. By selecting a photon cluster in the fiducial region of the ECal, the energy resolution of the electron (position given by the track projection at the ECal) could be measured at various energies and characterized. For each mm in the vertical position relative to the edge at the beam gap, it was found that the second parameter of the energy resolution described by Equation (4.2.17) (of the form b/\sqrt{E}) was strongly correlated with the position. By fixing the other two terms to the values in the fiducial region, the value of the b parameter was studied as a function of position. [13] The final characterization of this value relative to the beam gap edge is shown in Figure 4.2.18. [1]

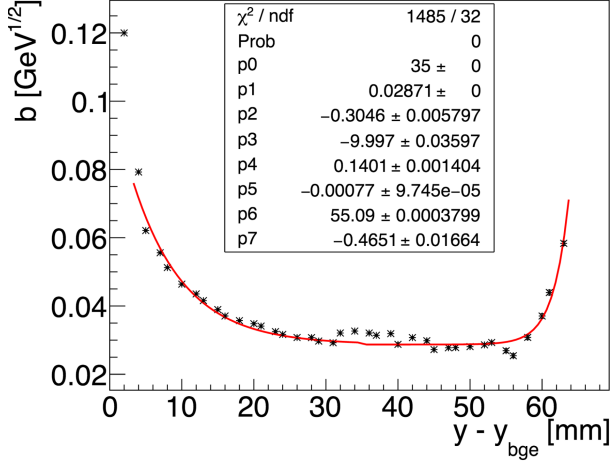


FIG. 4.2.19: The stochastic parameter b (corresponding to the $1/\sqrt{E}$ term) of the energy resolution description is shown as a function of the vertical position relative to the ECal beam gap edge. The fit function is shown in Equation (4.2.18).

The function that describes how Equation (4.2.18) is modified to account for the position relative to the inner beam gap edge is shown in Equation (4.2.18).

$$\begin{aligned} \frac{\sigma_E}{E} (\%) &= \frac{1.62}{E} \oplus \frac{b(y - y_{bge})}{\sqrt{E}} \oplus 2.5 \\ B(y < p_0) &= p_1 - p_2 e^{-(y-p_3)p_4} \\ B(y > p_0) &= p_1 - p_5 e^{-(y-p_6)p_7} \end{aligned} \quad (4.2.18)$$

The energy resolution parameterizations are reliable down to approximately half a crystal width away from the edge of the crystal, but the energy is significantly deteriorating at about 10 mm from the edge of the crystal. [13]

4.2.7 TIMING CALIBRATION AND PERFORMANCE

The time obtained from the raw fitting of the waveform requires corrections in order to account for various crystal-to-crystal time offsets that can result due to time walk and differences in hardware (such as cable lengths). The overall time offset for each crystal can be corrected using the accelerator RF signal, and the time walk can be removed through study of hits and hit energies in a cluster versus that of the seed hit energy. The corrected individual crystal time is shown in Equation (4.2.19).

$$t = t_0 + \Delta t_{RF} + \Delta t_w(E) \quad (4.2.19)$$

In Equation (4.2.19), t_0 is the time calculated from fit to the raw ADC distribution of a crystal, Δt_{RF} is the hit time offset with the accelerator RF signal, and $\Delta t_w(E)$ is the energy-dependent time-walk correction. The accelerator has a an intrinsic frequency of 499 MHz, and the RF signal is sampled every 80 signals into Hall B. The RF signal in the hall is readout by two FADC250 channels. The raw waveform of the RF signal is shown in Figure 4.2.20.

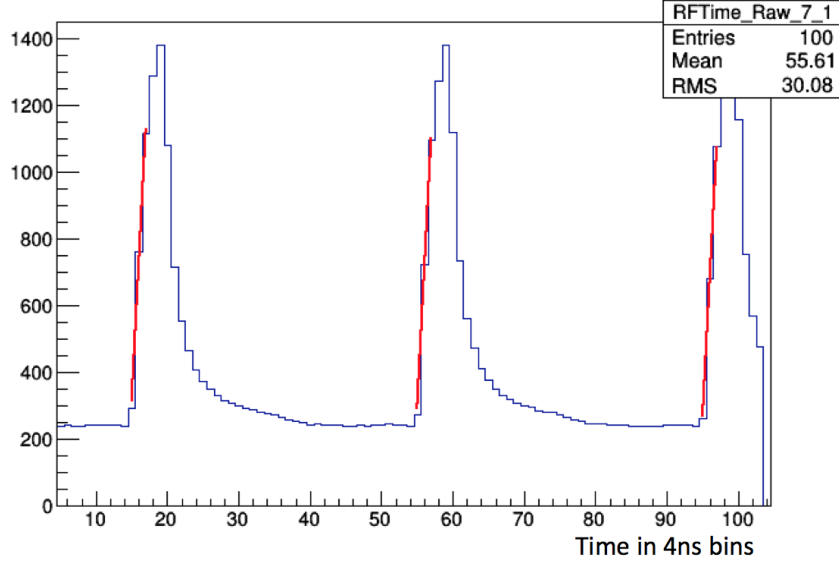


FIG. 4.2.20: The raw distribution of the RF signal is shown with a straight line fit to the leading edge of the signal.

The strategy to read off the time from the RF signal was chosen in order to minimize the measured intrinsic resolution of the FADC modules. After identifying the peak bin (4 ns per bin), the pedestal was calculated by averaging the values in 4 bins occurring at 6 to 9 samples prior to the peak. The threshold used in selecting the fitting points was found by calculating the 1/3 height between the averaged pedestal and the peak. The points for the straight line fit were then chosen as the last point below this threshold and the next two points above the threshold. These points were chosen due to the linear uniformity of the pulse away from the peak bin. The time that was used from this fit was at the half height between the pedestal and the peak. This combination of parameters minimized the width of the time difference distribution between the RF signals in the two FADC channels as shown in Figure 4.2.21.

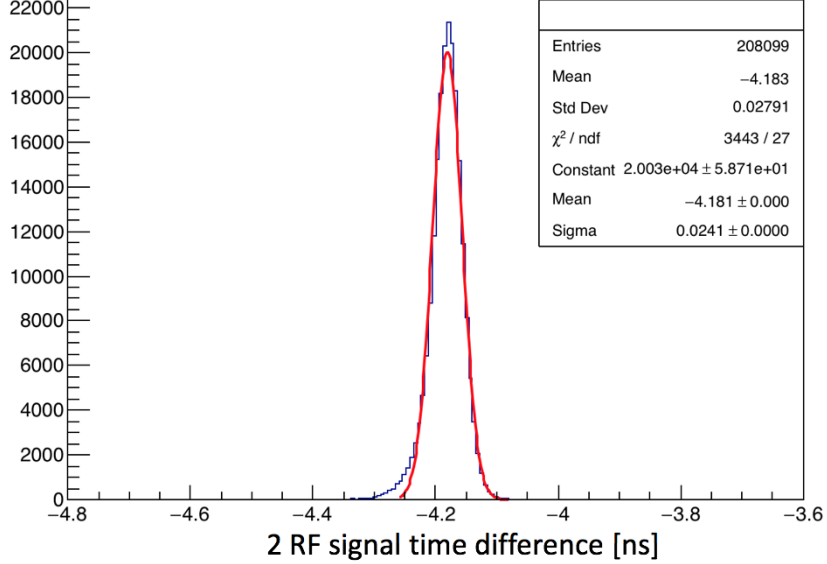


FIG. 4.2.21: The intrinsic time resolution of the FADC modules can be obtained by the width of the two RF signal time difference to be approximately 24 ps.

The internal time resolution of the FADC modules was measured to be approximately 24 ps from the width of the time difference between the two RF signals. The individual crystal module time offsets are measured with respect to the accelerator RF time. For time offsets less than 2 ns, or the time between electron bunches from the accelerator, we calculate the fine time offset per crystal as shown in Equation (4.2.20).

$$\Delta t_{fine} = \text{modulo}(t_0 - t_{RF} + N \times 2.004, 2.004) - 1.002 \text{ ns} \quad (4.2.20)$$

In Equation (4.2.20), t_0 is the time for the crystal as reported from pulse-fitting, t_{RF} is the reported RF time, and N is an arbitrarily large integer to shift the distribution to all positive values. 2.004 ns pertains to 499 MHz accelerator RF frequency. Before applying Equation (4.2.20), we observe the beam bunch structure in the time difference between the crystal hits and the RF time in Figure 4.2.22.

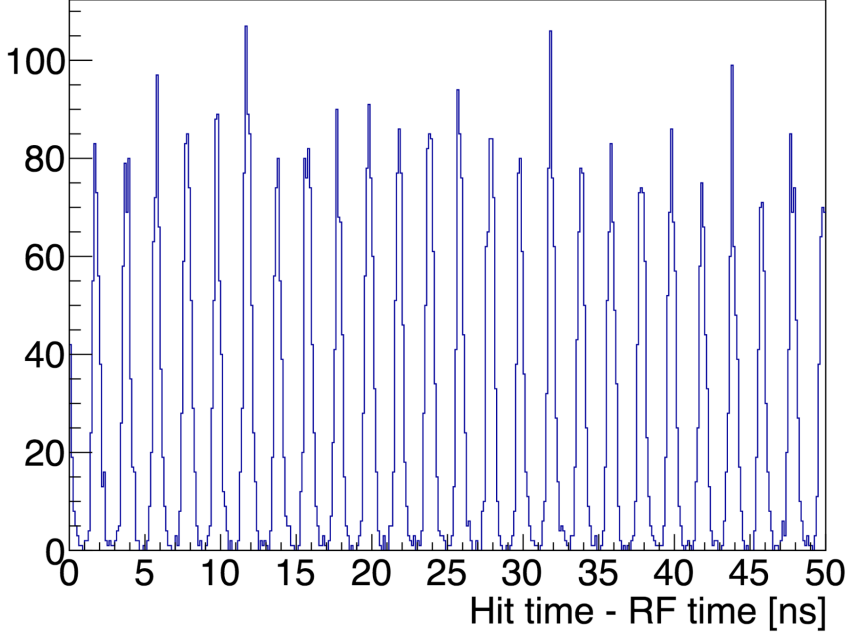


FIG. 4.2.22: From the time difference between ECal hits and the RF time, electron beam bunch structure is seen to occur at approximately 2 ns, consistent with known accelerator frequency.

By applying Equation (4.2.20) to Figure 4.2.22, we align all of the signals and see the fine offset of each module with respect to the RF time. This technique only shows the offset component that is less than 2 ns and results in all crystals being aligned to the nearest $2n$ ns, where n is any integer.

To fully align the crystals, we choose a crystal to align with RF signal at 0, and then align all other crystals with respect to this crystal. Because the primary trigger for HPS is a cluster pairs trigger, we can compare the time difference between clusters to make this correction. The time of the highest energy hit in a cluster was used to set the time for the cluster. Comparison studies exploring the use of an energy-weighted cluster time using the hit times in a cluster found no significant difference due to the seed hit energy dominating the time distribution and producing the same results as if one had used the time from the seed hit only. Well-correlated pairs of clusters were selected by looking for pairs with an energy sum equal to the beam energy and an energy difference of less than 200 MeV. The times for both clusters must have occurred in the 30-70 ns time window for the Engineering Run which was the optimal time window for triggered events. The time difference correction between two pairs of clusters after the fine time offset correction is shown in Figure 4.2.23.

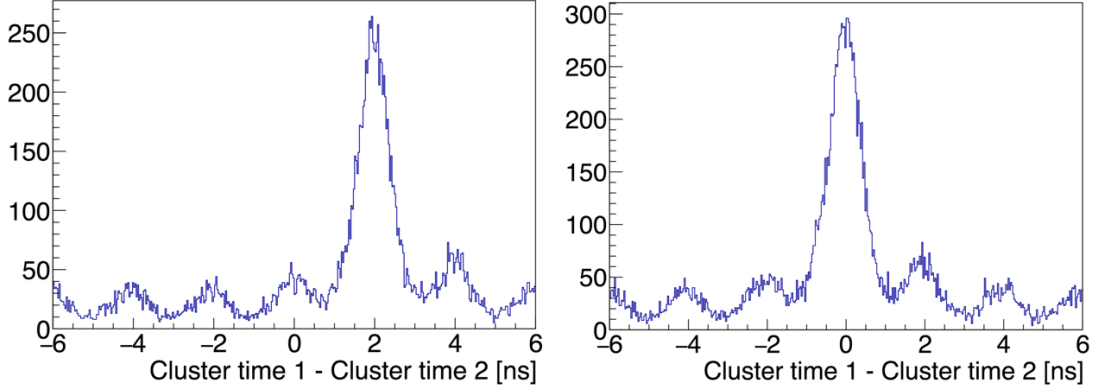


FIG. 4.2.23: After correcting all clusters with the fine timing offset correction, clusters are aligned to the nearest 2 ns time offset with respect to the RF signal. Shown on the left is a cluster pair that has an overall 2 ns time difference that needs to be accounted for in the final offset with the RF time. The plot on the right shows a different cluster pair with an offset centered at 0.

In Figure 4.2.23, a large 2 ns offset between a cluster pair is seen on the left prior to this step in the timing correction with respect to the RF signal. A different cluster pair, shown on the right, is seen to have no overall time offset that needs to be accounted for with respect to the RF time.

After correcting for the time offsets of all crystals with respect to the RF time, an energy-dependent correction, known as the time walk correction, must be accounted for. Time walk is the time difference of a signal crossing threshold in an ADC due to the finite rise time of the leading edge and the difference in signal amplitudes for particles of different energies. The effect causes particles of lower energy to cross the threshold later in time than particles of higher energy. This effect is not physical and can be removed by studying the time difference between hits in a cluster versus the seed hit as a function of the hit energy. Pulse fitting of the raw signal removes most of the time walk when compared to other methods that can be used to obtain a hit time. In the Engineering Run data, the seed hit was greater than 400 MeV and provided a reasonable threshold against which to compare hit times at lower energies. For the Physics Run data, the time walk correction was able to use a much higher seed hit threshold of 1 GeV, and the energy-dependence could be extended to higher energies. The time walk can be extracted from the comparison of the the hit times within a cluster as shown in Figure 4.2.24.

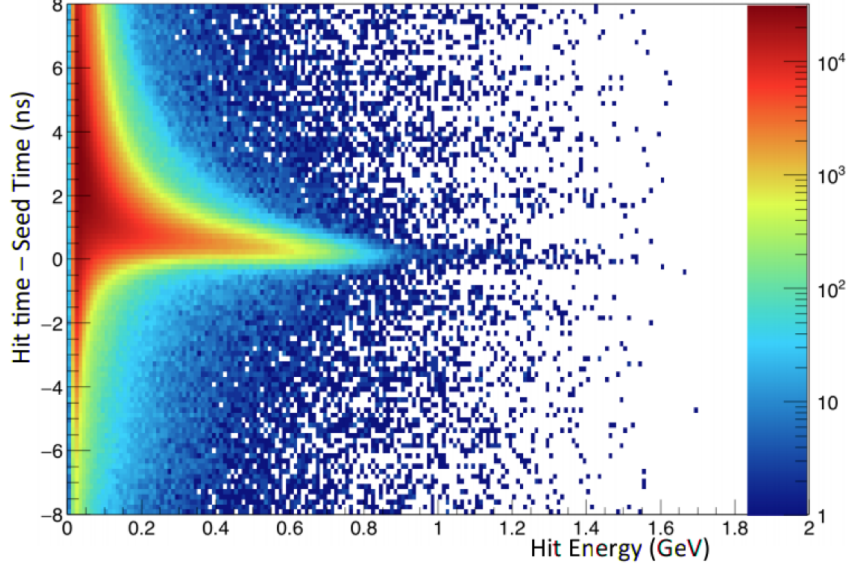


FIG. 4.2.24: The time walk correction for the 2016 data can be extracted from the difference of hit times in a cluster versus the seed hit time as a function of the the hit energy.

The time walk correction found from the Physics Run data is shown in Figure 4.2.25.

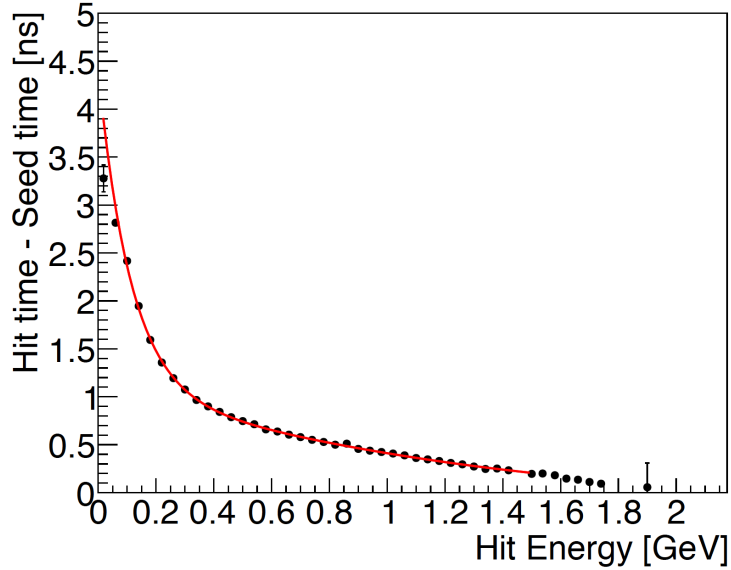


FIG. 4.2.25: The time walk correction for the Physics Run data was found by comparing the time difference between hits in a cluster versus the seed hit time.

The time walk shown in Figure 4.2.25 is described by the form in Equation (4.2.21).

$$\Delta_{t_{walk}} = e^{p_0 + p_1 E} + p_2 + p_3 E + p_4 E^2 \quad (4.2.21)$$

After removing all crystal-to-crystal time offsets and applying the energy-dependent time walk correction to all modules, the resulting time resolution for all energies is shown in Figure 4.2.26.

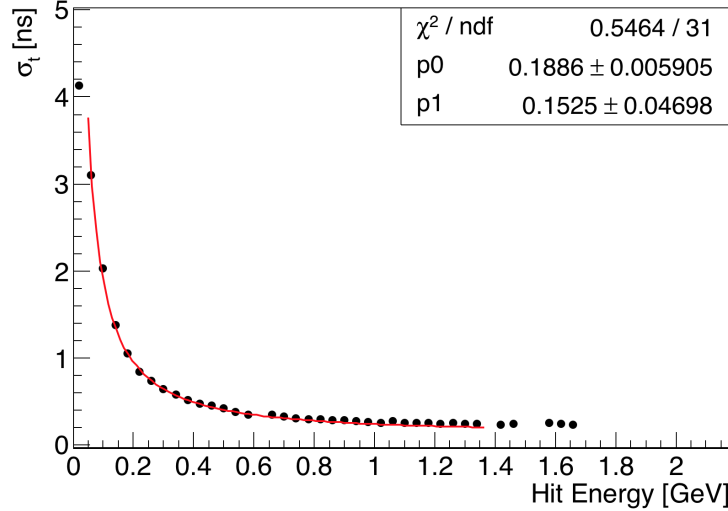


FIG. 4.2.26: The time resolution as a function of energy is shown.

The time resolution as a function of hit energy shown in Figure 4.2.26 is described by Equation (??)

$$\sigma_t [\text{ns}] = \frac{p_0}{E} \oplus p_1 \quad (4.2.22)$$

The measured time resolution for the time difference between two clusters is shown in Figure 4.2.27.

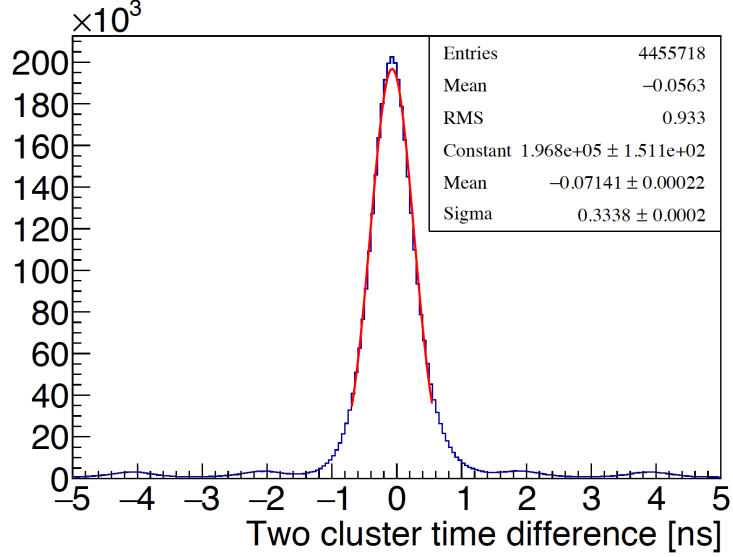


FIG. 4.2.27: The time difference between two clusters is shown. The energies sum to greater than 80% of the beam energy and have a resulting resolution of approximately 330 ps .

As shown in Figure 4.2.27, for two clusters that have an energy sum greater than 80% the beam energy in 2016, the resolution is approximately 330 ps. For the Engineering Run at a lower beam energy, the resolution of the time difference between two clusters was found to be approximately 470 ps.

CHAPTER 5

SEARCHING FOR DISPLACED VERTICES

5.1 DATASETS

5.2 MONTE CARLO SIMULATION

5.2.1 RADIATIVE FRACTION

5.2.2 VERTEX RECONSTRUCTION EFFICIENCIES, ϵ_{VTX}

5.2.3 MASS RESOLUTION

5.3 VERTEX CUTS

5.3.1 SVT AT NOMINAL POSITION

5.3.2 SVT AT OPEN POSITION

The following section consists of three different datasets used to measure a combined 0.5 mm reach. The 0.5 mm data was recorded during stable beam times when the SVT bias voltage was on, and the SVT layer 1 was positioned at ± 0.5 mm from the beam.

The 1.5 mm datasets consist of the data that was taken over approximately 0.5 beam days with the first layer of the SVT at 1.5 mm from the beam. Because this run was the engineering run, the beam position and stability had to be fully understood before moving the SVT in to its nominal position at 0.5 mm from the beam.

CHAPTER 6

VERTEX SEARCH RESULTS

6.1 BLINDED RESULTS AND PROJECTIONS

6.1.1 SVT AT NOMINAL POSITION

6.1.2 SVT AT OPEN POSITION

6.1.3 ESTIMATE OF CONTAMINATION BY ACCIDENTALS

6.2 UNBLINDED RESULTS

6.2.1 SVT AT NOMINAL POSITION

6.2.2 SVT AT OPEN POSITION

6.2.3 ESTIMATE OF CONTAMINATION BY ACCIDENTALS

6.3 REACH

CHAPTER 7

CONCLUSION

BIBLIOGRAPHY

- [1] I. Balossino et al, *The HPS electromagnetic calorimeter* Nuclear Instruments and Methods in Physics Research Section A Accelerators Spectrometers Detectors and Associated Equipment 854 October 2016
- [2] N. Baltzell et al., *The Heavy Photon Search beamline and its performance* Nuclear Instruments and Methods in Physics Research Section A Accelerators Spectrometers Detectors and Associated Equipment 859 December 2016
- [3] H. Szumila-Vance and M. Garçon, *HPS/ECal simulations: energy and position reconstruction for electrons, positrons and photons*, HPS-Note 2014-001.
- [4] HPS Collaboration, *Heavy Photon Search at Jefferson Laboratory: proposal for the 2014-2015 run* May 10, 2013.
- [5] R. Kazimi, *Simultaneous Four-Hall Operation for 12 GeV CEBAF* In Proceedings, 4th International Particle Accelerator Conference (IPAC 2013), page WEPFI085,2013.
- [6] V.A. Batarin et al., *Correlation of beam electron and LED signal losses under irradiation and long-term recovery of lead tungstate crystals* Nucl. Instrum. Meth. A 550 (2005) 543-550.
- [7] A. Celentano et al., *Design and realization of a facility for the characterization of Silicon Avalanche PhotoDiodes*, JINST 9 (2014) T09002, arXiv:1504.01589.
- [8] CLAS12 Collaboration, *CLAS12 Forward Tagger (FT) Technical Design Report*, CLAS12, (2012), <https://www.ge.infn.it/batta/jlab/ft-tdr.2.0.pdf>
- [9] K.A.Olive et al.[Particle Data Group Collaboration], Chin. Phys. C 38, 090001 (2014).
- [10] A. Celentano and G. Charles, HPS-NOTE 2014-002.
- [11] N. Baltzell ECal Pulse Fitting, HPS-NOTE 2015-010.
- [12] H. Szumila-Vance Ecal Timing Calibration for the Spring 2015 Engineering Run, HPS-NOTE 2015-011.
- [13] H. Szumila-Vance HPS Energy Calibration for the Spring 2015 Engineering Run, HPS-NOTE 2016-002.

- [14] B. Holdom, Physics Letters B 166 (1986) 196.
- [15] B. Holdom, Physics Letters B 178 (1986) 65.
- [16] PANDA EMC-TDR, October 2008.
- [17] Jia Liu, Neal Weiner, and Wei Xue. Signals of a Light Dark Force in the Galactic Center. In: Journal of High Energy Physics 2015.8 (Aug. 2015). issn: 1029-8479. doi: 10.1007/JHEP08(2015)050. arXiv: 1412.1485.
- [18] <https://arxiv.org/pdf/0906.0580.pdf>
- [19] J. R. Batley et al. (NA48/2), Phys. Lett. B746, 178 (2015), 1504.00607.
- [20] <https://arxiv.org/pdf/1404.5502.pdf>
- [21] <https://arxiv.org/pdf/1702.03327.pdf>
- [22] <https://arxiv.org/pdf/0906.0580.pdf>
- [23] Orsaybd)
- [24] Dark Sectors 2016 Community Workshop report

APPENDIX A

VITA

Holly Szumila-Vance
Department of Physics
Old Dominion University
Norfolk, VA 23529

The text of the Vita goes here.